ADVANCED ENERGY MATERIALS
www.advenergymat.de

Perovskite-Inspired $Cs_2AgBi_2I_9$: A Promising Photovoltaic Absorber for Diverse Indoor Environments

Mokurala Krishnaiah, Kuntal Singh, Sanchi Monga, Akash Tripathi, Sougata Karmakar, Ramesh Kumar, Christos Tyrpenou, George Volonakis, Debjit Manna, Paavo Mäkinen, K. V. Adarsh, Saswata Bhattacharya, G. Krishnamurthy Grandhi, K. D. M. Rao,* and Paola Vivo**

Indoor photovoltaics (IPVs) using low-toxicity bismuth-based perovskite-inspired materials (PIMs) can potentially power the growing number of Internet of Things devices sustainably. However, modest indoor power conversion efficiency (PCE) values are reported due to intrinsic limitations of PIMs, particularly regarding charge carrier separation and transport. Herein, polycrystalline $Cs_2AgBi_2I_9$ thin films are developed with high phase purity and study their fundamental structural and photophysical properties. The comprehensive experimental and computational study reveals unique optoelectronic properties of $Cs_2AgBi_2I_9$ compared to other bismuth-containing PIMs, including weak electron-phonon coupling and low exciton binding energy (40 meV). This study also demonstrates the feasibility of large and highly mobile polaron formation in $Cs_2AgBi_2I_9$, supported by the observation of a phonon bottleneck and a delayed hot carrier lifetime of over 200 ps, which suggests enhanced defect tolerance and transport properties. Motivated by the suitable bandgap of this absorber (1.78 eV), the first $Cs_2AgBi_2I_9$-based IPVs are developed, achieving a PCE of ≈8% at 1000 lux. Notably, the devices maintain high performance across various indoor environments with white LED color temperatures ranging from 2700 to 6500 K. The calculated theoretical PCE limit of >40% and the promising operational stability position $Cs_2AgBi_2I_9$ as one of the most intriguing candidates for sustainable IPVs.

1. Introduction

The Internet of Things (IoTs), predominantly powered by batteries, is witnessing rapid growth. By 2032, it is estimated that ≈34 billion devices will be integrated into the IoT ecosystem, reflecting a 10% compound annual growth rate.[1] As a significant portion of IoT sensors operate in indoor environments, indoor photovoltaics (IPVs) present a viable and sustainable energy harvesting solution by efficiently converting ambient light into electricity, thereby reducing battery dependence and minimizing associated waste.[2] White light-emitting diodes (WLEDs) have become the leading choice among various artificial light sources, surpassing options like compact fluorescent lamps. The color temperatures of indoor WLEDs vary from <3300 K (warm white light), to >5300 K (cold white light).[3,4] While warm WLEDs are typically chosen for living rooms and bedrooms in residential settings to

M. Krishnaiah, D. Manna, P. Mäkinen, G. K. Grandhi, P. Vivo
Hybrid Solar Cells
Faculty of Engineering and Natural Sciences
Tampere University
P.O. Box 541, Tampere FI-33720, Finland
E-mail: paola.vivo@tuni.fi

K. Singh, S. Karmakar, K. D. M. Rao
School of Applied & Interdisciplinary Sciences
Indian Association for the Cultivation of Science
Jadavpur, Kolkata 700032, India
E-mail: saiskdmrao@iacs.res.in

The ORCID identification number(s) for the author(s) of this article can be found under https://doi.org/10.1002/aenm.202404547

DOI: 10.1002/aenm.202404547

S. Monga, S. Bhattacharya
Department of Physics
Indian Institute of Technology Delhi
New Delhi 110016, India
E-mail: saswata@physics.iitd.ac.in

A. Tripathi, K. V. Adarsh
Department of Physics
Indian Institute of Science Education and Research
Bhopal, Madhya Pradesh 462066, India

R. Kumar
Department of Chemistry
Ångström Laboratory
Uppsala University
Box 523, Uppsala SE 75120, Sweden

C. Tyrpenou, G. Volonakis
ENSCR
INSA Rennes
CNRS
ISCR (Institut des Sciences Chimiques de Rennes)
Univ Rennes
Rennes UMR 6226, France

create a relaxing and calming atmosphere, cool WLEDs are preferred in work environments like classrooms and offices, as the dominant blue light component helps increase alertness.[3,4] Typically, the performance of IPV devices varies with different color temperatures, depending on whether the light-absorbing layer absorbs more strongly on the blue or red side of the WLED emission spectrum.[3–6] Therefore, developing versatile IPV absorbers that maintain stable performance under indoor environments with varying color temperatures of the light sources is crucial for advancing IPV technologies, yet largely overlooked in the literature.

Advanced thin-film photovoltaic (PV) technologies, such as organic photovoltaics, dye-sensitized photovoltaics, and lead-halide perovskites (LHPs), have demonstrated considerable potential in efficiently harvesting low-intensity indoor light.[7] LHPs, with power conversion efficiencies surpassing 26%,[8] exhibit remarkable photovoltaic performance under indoor lighting conditions. Their wide bandgap (≈1.7–1.9 eV) facilitates high indoor power conversion efficiencies (PCEs), reaching values exceeding 44%[9] and an open-circuit voltage (V_{OC}) of 1.25 eV under 1000 lux illumination.[10] Although recent reports suggest that LHPs can comply with international regulatory standards, such as the EU Restriction of Hazardous Substances (RoHS) directive, by maintaining lead (Pb) content below the 1000 ppm threshold,[11] the use of thin, flexible substrates for specific IoT sensors can lead to an increase in Pb levels beyond this limit.[12] Furthermore, the acceptance of Pb-containing devices operating in close proximity to the end user is restricted due to health and safety concerns. Consequently, despite their exceptional performance, LHPs are not entirely suitable for sustainable indoor PV applications.

Low-toxicity alternatives of LHPs, such as pnictogen based perovskite-inspired materials (PIMs) containing Group VA cations like Bi(III) and Sb(III), have garnered significant interest for IPV applications.[13–15] These materials offer high polarizability, necessary for good defect tolerance, and ns^2 valence electronic configuration, similar to Pb^{2+} in LHPs. Bismuth (Bi) is particularly interesting for its environmentally benign nature.[16] Additionally, the wide bandgaps (≈1.8–2.0 eV) of the pnictogen based PIMs result in theoretical indoor PCEs between 50% and 60%.[13–15] Although research is still in its early phases, recent reports of IPVs using these low-toxicity PIMs show promising indoor PCE values between 5% and 10%.[14] However, it is challenging to compare the performance of PIM-based IPVs from various studies due to the lack of standardized comparison methods, including standard IPV cells and the general reliance on lux meters instead of spectrometers.[17] In several cases, the reported short-circuit current density (J_{SC}) values for LHPs even exceed the theoretical limits.[10] This can mainly be attributed to the overestimation of photocurrent values from current density (*J*)-voltage (*V*) measurements[18] or *J*-*V* measurements performed at higher irradiance levels than those expected for indoor standard testing conditions (ISTC).[17,19] In most reports on PIMs, there is either a lack of photocurrent verification[13,20–23] or the use of higher irradiance values than those specified in ISTC.[21,23–25]

Bi- and Sb-based PIM IPV devices encounter significant current and voltage losses primarily attributed to non-radiative recombination processes and strong carrier localization effects.[26,27] The inherently soft lattice structures of LHPs and halide PIMs facilitate the formation of polarons – quasiparticles that arise from interactions between charge carriers and lattice vibrations.[26,28–30] In 3D LHPs, large polarons exhibit weak carrier-phonon coupling, which enables coherent charge carrier-lattice interactions, thereby enhancing carrier lifetimes and mobility.[31–34] Conversely, small polarons, which are commonly observed in low-dimensional Bi- and Sb-PIMs, are characterized by strong carrier-phonon coupling, resulting in localized exciton emissions and significantly reduced charge carrier mobilities.[27,35]

To address these limitations, compositional engineering has emerged as an effective strategy for minimizing recombination losses and fine-tuning the bandgap to achieve stable device performance in both LHPs and PIMs.[9,13,21,25,36] In our recent study, the partial substitution of Cs with Ag in $Cs_3Bi_2I_9$ effectively transformed the material from a highly-confined 0D structure into a 2D quaternary $Cs_2AgBi_2I_9$.[32] Single-crystal samples of $Cs_2AgBi_2I_9$ exhibit a suitable wide bandgap of 1.72 eV,[32] along with a high carrier mobility-lifetime product ($\mu\tau$) of 3.4×10^{-3} cm^2 V^{-1} and a low exciton binding energy, which collectively facilitate efficient charge carrier generation and transport. The resultant hot-carrier bottleneck effect further prolongs hot-carrier lifetimes, positioning $Cs_2AgBi_2I_9$ as a highly promising candidate for IPV applications.

In this work, we use a direct solution spin-coating method to successfully prepare thin films of polycrystalline $Cs_2AgBi_2I_9$ films, as confirmed by structural and compositional analyses. The $Cs_2AgBi_2I_9$ thin films exhibit a smaller exciton binding energy and weaker exciton-phonon coupling than many halide PIMs. Theoretical calculations reveal that $Cs_2AgBi_2I_9$ has significantly larger polaron characteristics, including size and mobility, compared to $Cs_3Bi_2I_9$ (CBI). These findings are experimentally validated through temperature-dependent time-resolved photoluminescence (TRPL) and electrical resistance measurements. Ultrafast transient absorption (TA) spectroscopy further indicates a phonon bottleneck, confirming large polaron formation with a delayed hot carrier lifetime (>200 ps) due to carrier-lattice Fröhlich interaction, protecting charge carriers from defect trapping. We fabricate PV devices incorporating $Cs_2AgBi_2I_9$ as the light-absorbing layer, which demonstrates nearly a tenfold improvement in PCE under solar illumination compared to CBI devices. Notably, the wide bandgap $Cs_2AgBi_2I_9$ ensures the highest indoor PCE under 1000 lux WLED illumination (color temperature 6500 K; ISTC irradiance). Our calculations of the spectroscopic limited maximum efficiency (i-SLME), combined with remarkable indoor operational stability, highlight the future IPV potential of $Cs_2AgBi_2I_9$ absorber. Finally, we identify strategies to further enhance indoor PCE values toward the i-SLME limit.

2. Results and Discussion

2.1. Structural, Compositional, and Photophysical Properties

The fabrication of $Cs_2AgBi_2I_9$ and CBI thin films through solution processing is detailed in the Experimental Section. Structural analysis using powder X-ray diffraction (PXRD) and subsequent Rietveld refinement ($R_w = 2.9$) confirmed that $Cs_2AgBi_2I_9$ adopts a hexagonal structure (space group P63/mmc) with lattice parameters $a = b = 8.4137$ Å, $c = 21.1910$ Å, and a unit cell volume of 1299.14 $Å^3$ (**Figure 1a**). The Ag-I bond lengths in $Cs_2AgBi_2I_9$

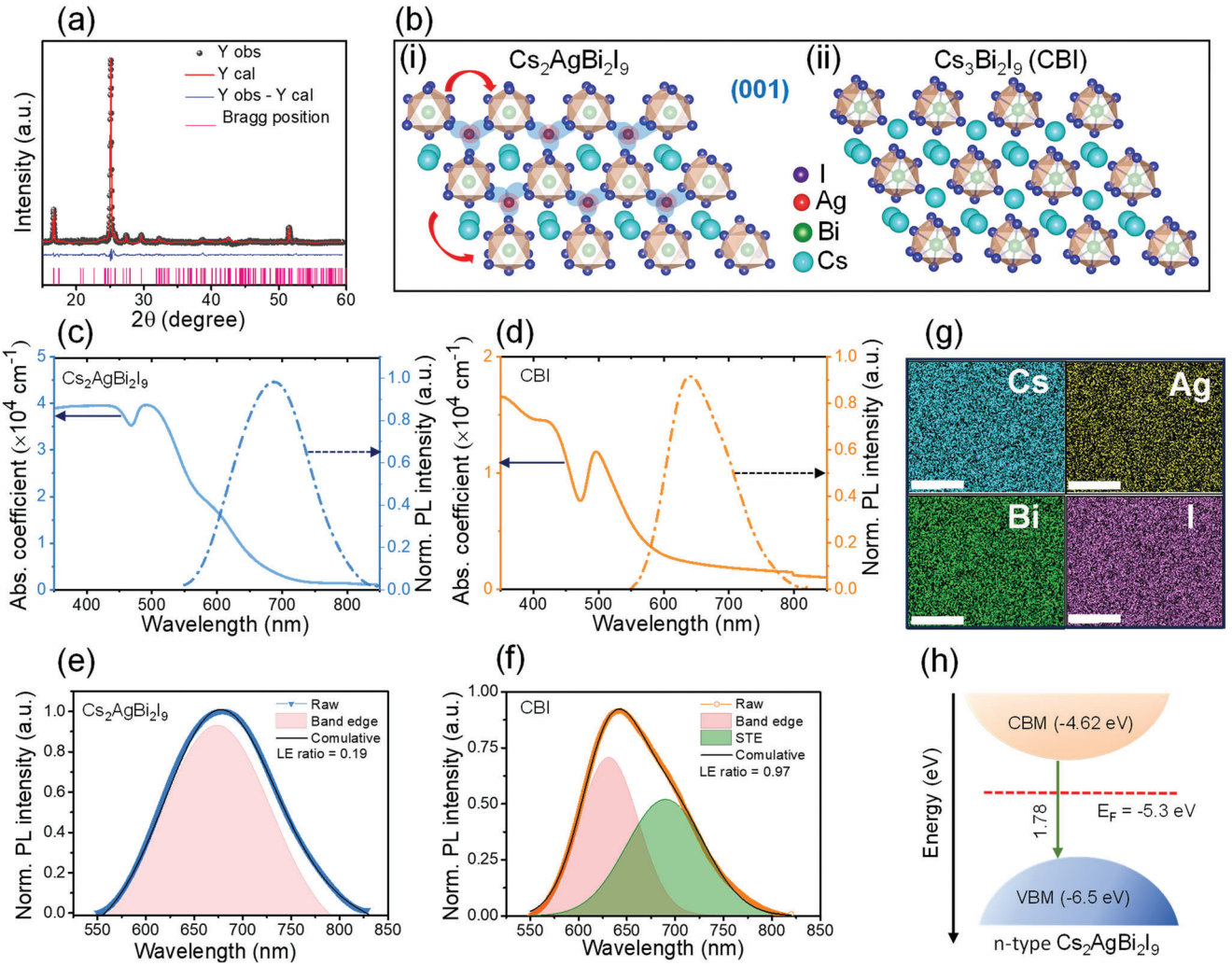

Figure 1. Comparison of structural and optical properties of $Cs_2AgBi_2I_9$ versus CBI thin films. a) Rietveld refinement of the room temperature powder X-ray diffraction (PXRD) pattern of $Cs_2AgBi_2I_9$ film. The black spheres represent the experimental PXRD pattern. The Rietveld fit and the difference between the fit and experimental patterns are shown as red and blue lines, respectively. The Bragg planes of the $Cs_2AgBi_2I_9$ crystal are represented by pink bars in the bottom panels. Structural representation of b-i) $Cs_2AgBi_2I_9$ and (b-ii) CBI viewed along the c-axis (perpendicular to the (001) plane). Blue and red contours in the $Cs_2AgBi_2I_9$ structure highlight the orbital overlap between I-6p and Ag-5s orbitals, respectively. UV–vis absorption coefficient and PL spectra of (c) $Cs_2AgBi_2I_9$ and (d) CBI thin films. Deconvolution of room temperature PL spectra of (e) $Cs_2AgBi_2I_9$ and (f) CBI thin film samples. The red and green shaded areas represent band-edge emission and STE emission, respectively. (g) Energy-dispersive X-ray mapping of $Cs_2AgBi_2I_9$ thin film with constituent elements. (h) Schematic representation of the band energy diagram of $Cs_2AgBi_2I_9$ estimated from ultraviolet photoelectron spectroscopy (UPS).

are shorter than the Cs-I distances in CBI (see Table S1, Supporting Information), Substituting Cs with Ag facilitates an overlap between I 6p and Ag 5s orbitals, leading to a more interconnected $[Bi_2I_9]^{3-}$ network along the (001) plane. This interaction promotes a transition from a 0D (CBI) to a 2D electronic structure in $Cs_2AgBi_2I_9$, as illustrated in Figure 1b,c. This enhancement in electronic dimensionality through Ag-I orbital overlap is absent in CBI and is expected to result in improved photocarrier extraction, making $Cs_2AgBi_2I_9$ highly promising for optoelectronic applications.

The UV–vis absorption and photoluminescence (PL) spectra (Figures 1d–f) revealed that $Cs_2AgBi_2I_9$ exhibits a redshifted absorption onset at 690 nm compared to the 580 nm onset observed for CBI. The optical indirect bandgaps (direct bandgaps) for $Cs_2AgBi_2I_9$ and CBI thin films were estimated from Tauc plots (Figure S1, Supporting Information) to be 1.78 eV (1.89 eV) and 2.11 eV (2.21 eV), respectively. This implies an energy difference of ≈0.1 eV between the direct and indirect bandgaps, suggesting a quasi-direct bandgap nature of the two materials. $Cs_2AgBi_2I_9$ demonstrated a higher absorption coefficient, three times greater than that of CBI within the 350–580 nm range, indicating enhanced light absorption capabilities. The PL spectrum of $Cs_2AgBi_2I_9$ displayed a redshifted peak at 689 nm and a smaller Stokes shift compared to CBI. The skewness parameter is quantified using the low energy (LE) ratio,[37] defined as:

$$LE\ ratio = \frac{Low\ energy\ PL\ intensity}{Band\ edge\ PL\ intensity} = \frac{Low\ energy\ PL\ area}{Band\ edge\ PL\ area} \quad (1)$$

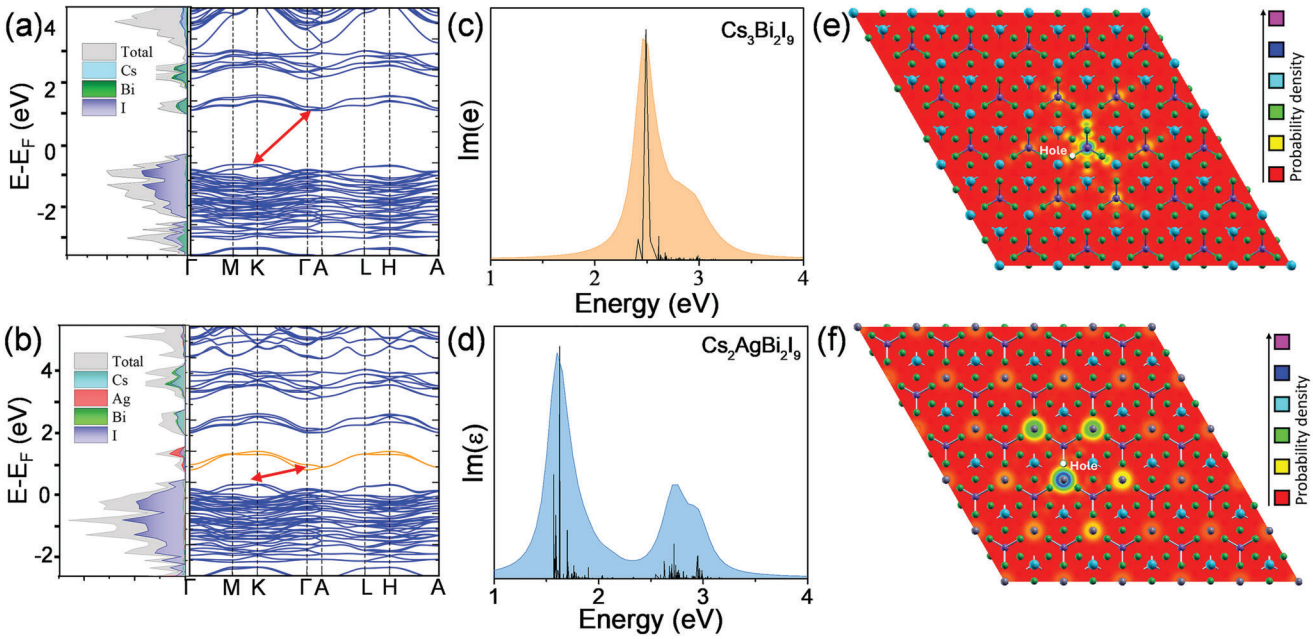

Figure 2. Electronic properties and excitonic characteristics of CBI and $Cs_2AgBi_2I_9$. a,b) Band structure and atom-projected density of states (DOS) for CBI and $Cs_2AgBi_2I_9$, respectively, calculated using PBE+SOC. c,d) Imaginary part of the dielectric function for CBI and $Cs_2AgBi_2I_9$, obtained from Bethe-Salpeter Equation (BSE) calculations, with the vertical lines representing the oscillator strength. e,f) Top view of the excitonic wavefunction of CBI and $Cs_2AgBi_2I_9$, respectively, in a 5 × 5 × 1 unit cell configuration.

When the LE ratio approaches zero, the peak is more symmetrical, indicating fewer self-trapped excitons (STEs). $Cs_2AgBi_2I_9$ showed an LE ratio of 0.17, while CBI exhibited a ratio of 0.97 (Figure 1e,f), suggesting significantly fewer STEs in $Cs_2AgBi_2I_9$, which is advantageous for PV applications.

Field emission scanning electron microscope (FE-SEM) images revealed dense, submicron-sized grains in both $Cs_2AgBi_2I_9$ and CBI films (Figure S2, Supporting Information), with the former showing a reduced number of pinholes. The SEM-EDX analysis (Figure 1g; Figure S3, Supporting Information) showed a nearly stoichiometric atomic composition for $Cs_2AgBi_2I_9$, indicating a uniform distribution of elements, while CBI also matched its theoretical stoichiometry (Figure S3, Supporting Information). Ultraviolet photoelectron spectroscopy (UPS) analysis (Figure 1h; Figure S4, Supporting Information) revealed n-type characteristics in $Cs_2AgBi_2I_9$ with Fermi level at −5.3 eV and valence band maximum (E_{VBM}) at −6.5 eV, contrasting with the p-type behavior observed in CBI.[32] The conduction band minimum, primarily formed by Ag-6s orbitals (as discussed in Section 2.2), shifts downward due to strong overlap between Ag-6s and I-5p orbitals, with minimal impact on the valence band maximum. This shift enhances electron conduction, resulting in n-type behavior.[38]

Raman spectroscopy (Figure S5, Supporting Information) identified seven distinct peaks for both films, with red-shifted peaks in $Cs_2AgBi_2I_9$ attributed to the substitution of larger Cs atoms with smaller Ag atoms, reducing the atomic mass (see Table S2, Supporting Information for details).[32,33] XRD and Raman spectra analyses revealed no additional peaks, confirming the absence of impurity phases in $Cs_2AgBi_2I_9$ thin films. These comprehensive structural, optical, and morphological analyses collectively guarantee superior optoelectronic properties of $Cs_2AgBi_2I_9$ compared to CBI. Additionally, we investigated the electronic band structure of $Cs_2AgBi_2I_9$ to understand the origin of its improved optoelectronic properties.

2.2. Electronic Band Structure Calculations and Visualization of the Large Polaron Formation

We computed the electronic band structures and atom-projected partial density of states (PDOS) for $Cs_3Bi_2I_9$ (CBI) and $Cs_2AgBi_2I_9$ using the generalized gradient approximation (GGA) with spin-orbit coupling (SOC). Both materials were found to be indirect bandgap semiconductors. This finding aligns with the experimental observation that their indirect bandgap values are slightly lower than their direct bandgap values. In CBI, the valence band maximum (VBM) is located at the M high-symmetry point, while the conduction band minimum (CBM) is positioned between the Γ and A points (**Figure 2a**). For $Cs_2AgBi_2I_9$, the VBM lies between the M and K points, and the CBM is at the Γ point (Figure 2b). The density of states (DOS) analysis shows that for both materials, the VBM is primarily composed of iodine (I) atomic orbitals. However, the CBM in CBI is mainly formed by hybridization of Bi and I orbitals, while in $Cs_2AgBi_2I_9$ it is dominated by Ag orbitals with a minor contribution from I (Figure 2a,b). The introduction of Ag in CBI lowers the CBM position but affects the VBM position negligibly, leading to a reduced bandgap of $Cs_2AgBi_2I_9$ compared to CBI. Parabolic fitting of the band edges allowed estimation of the effective masses of charge carriers (**Table 1**). The electrons have a lower effective mass than holes in both materials, which corresponds to higher

Table 1. Electronic static dielectric constant (ε_∞), total static dielectric constant (ε_o), and effective masses of electrons (m_e*) and holes (m_h*) expressed as multiples of the electron rest mass (m_o).

Material	ε_∞	ε_o	m_e*	m_h*
CBI	5.6	10.6	4	−9.8
$Cs_2AgBi_2I_9$	6.5	14.6	0.6	−2.1

electron mobility. The incorporation of Ag in CBI results in a further reduction of effective charge-carrier masses, promising an enhanced charge-carrier mobility in $Cs_2AgBi_2I_9$.

To include many-body effects, we conducted single-shot GW (G_oW_o) calculations, yielding bandgap values of 2.67 eV for CBI and 1.60 eV for $Cs_2AgBi_2I_9$. To account for electron-hole interactions, we applied the Bethe-Salpeter equation (BSE) method, which revealed optical bandgaps of 2.41 eV for CBI and 1.56 eV for $Cs_2AgBi_2I_9$ (Figure 2c,d). The exciton binding energies, calculated as the difference between the electronic (GW) and optical (BSE) bandgaps, were found to be 260 meV for CBI and 40 meV for $Cs_2AgBi_2I_9$. This indicates that CBI has strongly bound excitons, while $Cs_2AgBi_2I_9$ exhibits weakly bound Wannier-Mott excitons. We also determined the zero-frequency electronic dielectric constant (ε_∞) from BSE and the static ionic dielectric constant (ε_{ion}) using density functional perturbation theory (DFPT), allowing calculation of the total static dielectric constant (ε_o) (Table 1). The nearly four-fold lowered exciton binding energy in $Cs_2AgBi_2I_9$ compared to CBI can be attributed to its reduced effective charge-carrier masses and increased dielectric screening.

To visualize the excitonics, we calculated the excitonic spectra and mapped the electron probability density within a $5 \times 5 \times 1$ unit cell for the first bright exciton, fixing the hole at an iodine (I) atom due to the dominance of I atomic orbitals at the VBM. This analysis revealed a shift in the maximum electron probability density from Bi atoms in CBI (Figure 2e) to Ag atoms in $Cs_2AgBi_2I_9$ (Figure 2f). This indicates the significant impact of Ag substitution into CBI on the excitonic states, consistent with the density of states observations.

We further investigated the electron-phonon interactions in CBI and $Cs_2AgBi_2I_9$ using the Fröhlich polaron model. As charge carriers move through the lattice, their interaction with longitudinal optical phonons leads to the formation of polarons, which increase the effective mass of the carriers, thereby reducing mobility and affecting optoelectronic properties.[39,40] The strength of this electron-phonon coupling is quantified by the dimensionless Fröhlich parameter, α, as defined by Fröhlich's expression.[34]

$$\alpha = \left(\frac{1}{\varepsilon_\infty} - \frac{1}{\varepsilon_0}\right)\sqrt{\frac{R_\infty}{\hbar\omega_{LO}}}\sqrt{\frac{m^*}{m_0}} \quad (2)$$

where, ε_∞ and ε_o represent the electronic and total static dielectric constants, respectively. The effective masses of electrons (m_e*) and holes (m_h*) are expressed in units of the electron rest mass (m_o), and ω_{LO} is the longitudinal optical phonon frequency calculated via the athermal B scheme by Hellwarth et al.[41] CBI shows intermediate electron-phonon coupling, while $Cs_2AgBi_2I_9$ exhibits weak coupling (see Table 1). In the weak regime, large polarons extend over multiple unit cells, indicated by the larger polaron radius, r_f.[42] We estimated the upper limit of polaron mobility using Feynman's variational solution to the Fröhlich polaron Hamiltonian by integrating the polaron response function.[39,42,43] **Table 2** presents the values of ω_{LO}, α, r_f, and μ, indicating that $Cs_2AgBi_2I_9$ has significantly higher polaron mobility at 36.24 $cm^2\ V^{-1}\ s^{-1}$ compared to 1.67 $cm^2\ V^{-1}\ s^{-1}$ for CBI, which will ensure enhanced carrier transport. Our electrical resistivity measurements (see Figure S6 and Table S3, Supporting Information) indicate that $Cs_2AgBi_2I_9$ films have a resistivity of $8.53 \times 10^9\ \Omega$ cm, which is three orders of magnitude lower than that of CBI films ($6.52 \times 10^{12}\ \Omega$ cm).

2.3. Experimental Evidence of Exciton-Phonon Coupling

We conducted temperature-dependent PL measurements in the 100–300 K range to investigate exciton-phonon interactions in $Cs_2AgBi_2I_9$ thin films (**Figure 3a**). The exciton binding energy extracted from this data was 39.1 ± 5.5 meV (see Note S1, Supporting Information), closely matching our theoretical value, indicating its suitability for photovoltaic applications. Additionally, we calculated a Huang–Rhys parameter (S) of 12.05 and an effective phonon energy (E_{Ph}) of 31.8 meV (Figure 3b). The relatively low Huang-Rhys parameter, consistent with previous single-crystal studies,[32] suggests suppressed exciton self-trapping via lattice distortion in $Cs_2AgBi_2I_9$ compared to CBI (79.5) and $Cs_3Sb_2I_9$ (42.7),[44] as detailed in Note S2 (Supporting Information). We also determined the electron-longitudinal optical (LO) phonon coupling parameter (γ_{LO}) as 113.85 meV, similar to single-crystal samples,[32] which indicates low electron-phonon interaction and reduced STE formation in $Cs_2AgBi_2I_9$ (see Note S3, Supporting Information).

To further elucidate electron-phonon scattering on recombination dynamics, temperature-dependent time-correlated single-photon counting (TCSPC) measurements were performed between 180 K and 300 K (Figure 3d). The decay curves were fitted using a bi-exponential model. At room temperature, the decay is governed by the slow decay component, which diminishes as temperature decreases, with the fast decay component becoming dominant (Figure 3e). This shift suggests reduced electron-phonon interactions at lower temperatures. Both fast and slow decay lifetimes increased with rising temperature (Figure S7, Supporting Information), leading to a longer average lifetime, contrasting with other PIMs where lifetimes typically increase with decreasing temperature.[44,45] The slower decay at 300 K compared to 180 K in $Cs_2AgBi_2I_9$ is attributed to enhanced electron-phonon coupling through inelastic scattering, as increased phonon density facilitates coupling with excitons, slowing the carrier relaxation process.[46] The prolonged carrier lifetime at higher temperatures suggests the formation of larger polarons, which protect against carrier-carrier and carrier-defect

Table 2. Longitudinal optical phonon frequency (ω_{LO}), strength of electron-phonon coupling (α), polaron radius (r_f), and polaron mobility (μ).

Material	ω_{LO} [cm^{-1}]	α	Polaron radius r_f [Å]	μ [$cm^2\ V^{-1}\ s^{-1}$]
CBI	89.58	5.01	21	1.67
$Cs_2AgBi_2I_9$	95.36	2.14	34	36.24

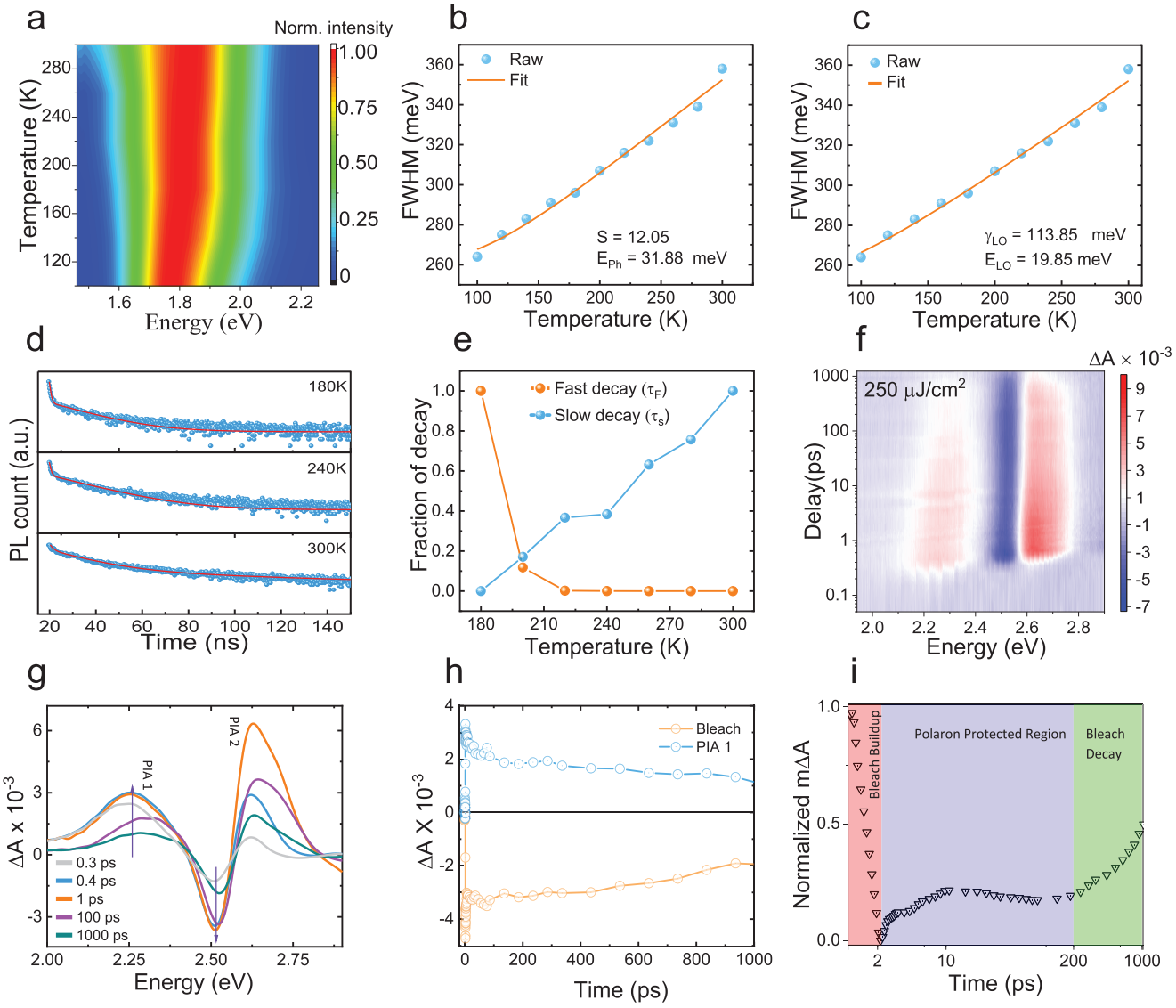

Figure 3. a) Contour plot of temperature-dependent PL evolution in $Cs_2AgBi_2I_9$ thin film. Least-square fitting of FWHM of the PL spectra as a function of temperature for determining electron-phonon coupling strength in $Cs_2AgBi_2I_9$ thin film with b) Toyozawa model and c) Rudin model. Here, blue dots represent experimental data, while orange color correspond to the fitted data with Toyozawa and Rudin models, respectively. d) Temperature-dependent TRPL decay curves of $Cs_2AgBi_2I_9$ thin film over a temperature range from 300 to 180 K. e) Normalized weightage of fast and slow decay components of $Cs_2AgBi_2I_9$. f) Contour plot of the room temperature transient absorption spectrum of $Cs_2AgBi_2I_9$ at an excitation fluence of 250 μJ cm^{-2}, illustrating the dynamic evolution of spectral features. g) Corresponding spectral slices at selected pump-probe delay times, showing PIA1 at lower energy and PIA2 at higher energy, along with excitonic bleach at 2.25 eV. h) Decay kinetics of PIA1 and the excitonic bleach, demonstrating their distinct temporal dynamics. i) Temporal evolution of the excitonic bleach, highlighting the buildup and saturation over time.

interactions, a concept further explored in the following section.[34]

We performed ultrafast transient absorption (TA) spectroscopy to probe the exciton-polaron dynamics in $Cs_2AgBi_2I_9$.[27] The TA measurements were conducted using above-bandgap pump pulses at 3.1 eV, with a fluence of 250 μJ cm^{-2}, which is higher than $Cs_2AgBi_2I_9$ bandgap. The contour plot of the TA data is presented in Figure 3f, and cross-sections at selected delay times are shown in Figure 3g. Additional TA data at fluences of 125 and 500 μJ cm^{-2} are included in Figures S8 and S9 (Supporting Information). To accurately identify the exciton energy, we analyzed the second derivative of the absorbance spectrum (Figure S10, Supporting Information), which matched well with the TA spectra. The TA spectrum revealed several critical features: 1) Instantaneous formation of a bleach signal at the excitonic position, accompanied by photoinduced absorption (PIA1) on the red side of the exciton energy and a delayed photoinduced absorption (PIA2) on the blue side. This combination of TA features—bleach at the exciton energy with PIAs on both sides—provides a clear framework for understanding the intricate excitonic behavior in $Cs_2AgBi_2I_9$. 2) The exciton bleach and PIA1 exhibit simultaneous growth, saturating within 0.5 ps, while PIA2 continues to

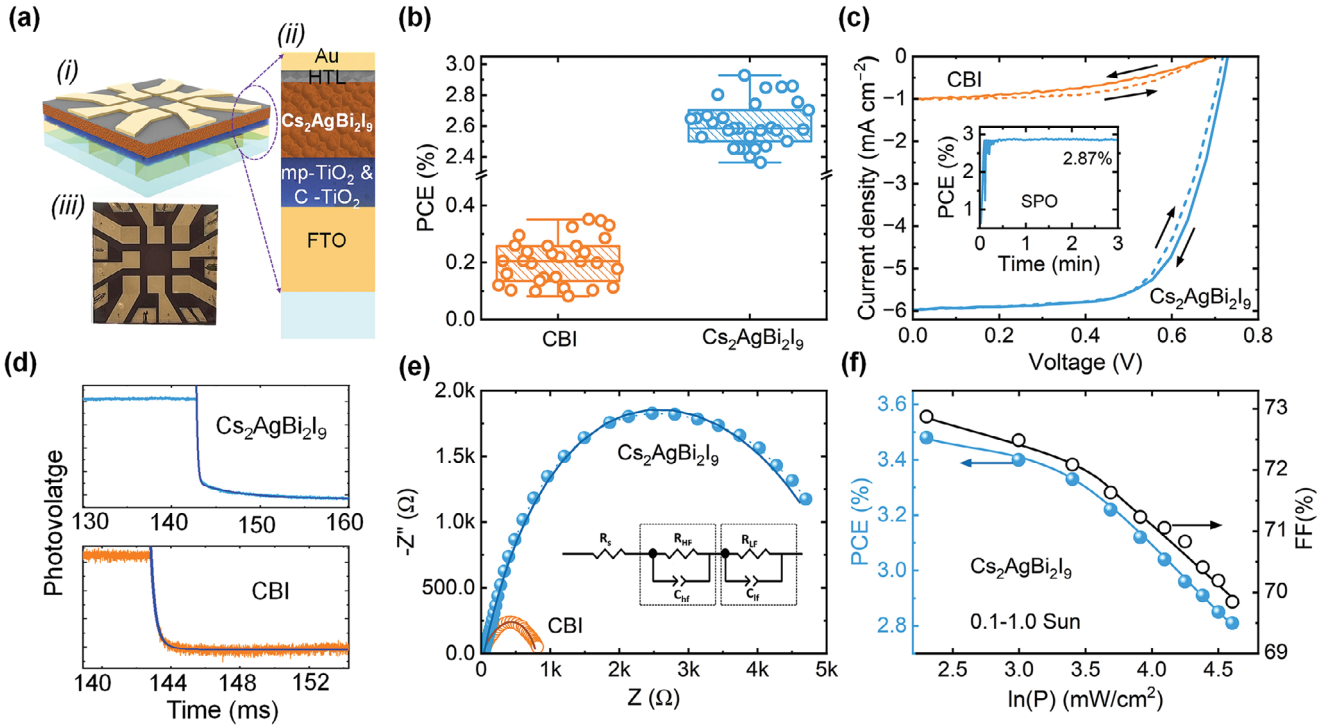

Figure 4. Evaluation of photovoltaic performance of CBI and $Cs_2AgBi_2I_9$ under 1-Sun (AM 1.5 G, 100 mW cm^{-2}). a) i-ii: schematic diagram of $Cs_2AgBi_2I_9$ device in *n-i-p* mesoscopic architecture (glass/FTO/c-TiO_2/mp-TiO_2/$Cs_2AgBi_2I_9$ or CBI/HTL/Au) and (iii) its optical image. b) Comparison of statistical distributions (obtained from 30 independent devices for reliable assessment) of the PCE of CBI and $Cs_2AgBi_2I_9$ devices. c) *J–V* curves (reverse and forward scans) of the CBI and $Cs_2AgBi_2I_9$ devices. d) Transient photovoltage (TPV) decay curves of CBI and $Cs_2AgBi_2I_9$ devices. e) EIS spectra of CBI and $Cs_2AgBi_2I_9$ devices. The corresponding inset shows the equivalent circuit used for fitting the EIS data. Here, two Randle circuits denoted by R_{HF}/C_{HF} and R_{LF}/C_{LF}, are related to high- and low frequency processes. f) The variations of PCE and FF of a $Cs_2AgBi_2I_9$ device with varying light intensities from 10 to 100 mW cm^{-2} (0.1–1.0 Sun).

grow beyond 0.5 ps, reaching saturation at 1 ps. The growth kinetics of the exciton bleach and PIA1 are nearly identical temporal dynamics (Figure 3h), suggesting they result from a derivative feature.[47] A combined effect of PIA_1 on the lower energy side and bleach on the higher energy side is indicative of polaron formation, further corroborated by their long lifetimes and synchronous decay.[48–51] The distinct saturation times of PIA1 and PIA2 indicate different underlying mechanisms, with PIA2 likely associated with the activation of higher-lying excited states. 3) Following their saturation, the exciton bleach, PIA1, and PIA2 remain stable for up to 200 ps before showing signs of decaying, demonstrating the robustness of exciton-polaron coupling and its influence on excited-state dynamics.[51] Figure 3g,h demonstrate that PIA1 and the bleach exhibit similar temporal dynamics, suggesting a shared exciton-polaron interaction mechanism. Furthermore, the complete bleach dynamics shown in Figure 3i, including delayed decay associated with large polarons,[51,52] imply that exciton-polaron interactions significantly govern the relaxation processes in $Cs_2AgBi_2I_9$, confirming the material potential for efficient optoelectronic device applications.

2.4. Photovoltaic Characterization

To demonstrate the impact of improved electronic dimensionality (from 0D to 2D) and large polaron formation on the charge transport properties of $Cs_2AgBi_2I_9$ compared to CBI, we fabricated *n-i-p* mesoscopic photovoltaic (PV) devices using these two Bi-PIMs as light absorber layers. Details on the device fabrication steps are provided in the Experimental section. For the device structure, we initially relied on the well-established TiO_2 and 2,2,7,7-tetrakis(N,N-di-p-methoxyphenylamine)-9,9-spirobifluorene (Spiro-OMeTAD) as the electron transport and hole transporting layers (ETL and HTL), respectively. The schematic diagram of the *n-i-p* mesoscopic device architecture (glass/FTO/c-TiO_2/mp-TiO_2/$Cs_2AgBi_2I_9$ or CBI/Spiro-OMeTAD/Au) is shown in **Figure** 4a. The distinct layers of the *n-i-p* mesoscopic device are clearly observed in the cross-sectional FE-SEM imaging of the complete $Cs_2AgBi_2I_9$ device (Figure S11, Supporting Information). The estimated thickness of the $Cs_2AgBi_2I_9$ light absorber layer is ≈385 nm (Figure S11, Supporting Information). The performance of both CBI and $Cs_2AgBi_2I_9$ devices was first evaluated under 1-Sun illumination (AM 1.5 G, 100 mW cm^{-2}) at room temperature. The champion CBI device achieved a PCE of 0.25% (refer to Figure S12, Supporting Information for the *J–V* curves and Figure S13 and Table S4, Supporting Information for statistical distribution of PV parameters). This efficiency falls within the typical range of ≈0.21–1.0% reported for CBI solar cells fabricated without any chemical modifications to the light-absorbing layer or device engineering,[53] i.e., when using a device structure similar to ours. The J_{SC} values of ≈0.8 mA cm^{-2} of the CBI devices can

Table 3. Average (30 devices) and the highest (in the brackets) photovoltaic parameter values of CBI and $Cs_2AgBi_2I_9$ devices with PPDT2FBT HTL under 1-Sun illumination.

Photovoltaic device	PCE [%]	FF [%]	J_{SC} [mA cm^{-2}]	V_{OC} [V]
CBI	0.20 ± 0.07 (0.37)	49.71 ± 6.37 (54.46)	0.53 ± 0.09 (0.99)	0.647 ± 0.048 (0.682)
$Cs_2AgBi_2I_9$	2.62 ± 0.30 (2.92)	66.60 ± 1.65 (67.2)	5.22 ± 0.46 (5.97)	0.763 ± 0.025 (0.729)

be attributed to their zero electronic dimensionality, resulting in poor charge transport. Conversely, the performance of the $Cs_2AgBi_2I_9$ devices is significantly better than that of CBI counterpart. A maximum PCE of 1.73% (Figure S14a, Supporting Information) was observed for the $Cs_2AgBi_2I_9$ solar cells, primarily due to a fourfold increase in the J_{SC} values compared to CBI devices, with the highest value reaching ≈3.32 mA cm^{-2} (see Figure S14a, Supporting Information). The enhanced photocurrents of the $Cs_2AgBi_2I_9$ devices compared to the CBI ones can be attributed to the high electronic dimensionality of $Cs_2AgBi_2I_9$, improved carrier mobility (refer to Table 2 for the theoretically predicted polaron mobilities between $Cs_2AgBi_2I_9$ and CBI, and Table S3 (Supporting Information) for the three-order magnitude difference in resistivity between the two materials), large polaron formation (refer to section 2.2), and reduced carrier self-trapping (refer to our spectroscopic data analysis, section 2.3). These factors collectively contribute to efficient charge transport within the $Cs_2AgBi_2I_9$ devices.

We further explored the importance of selecting a suitable HTL for maximizing the device performance. Conjugated conducting polymers have been explored as HTLs for LHP and chalcogenide PIM solar cells because of their high hole mobility, tunable energy levels, unique chemical interaction, and solution-processability.[54–56] We chose two of them, namely, poly[2,6-(4,4-bis-(2-ethylhexyl)-4H-cyclopenta[2,1-b;3,4-b']dithiophene)-alt-4,7(2,1,3-benzothiadiazole)] (PCPDTBT) and poly[(2,5-bis(2-hexyldecyloxy)-phenylene)-alt-(5,6-difluoro-4,7-di(thiophen-2-yl)benzo[c]-[1,2,5]-thiadiazole)] (PPDT2FBT). Figure 4b and Figure S14b (Supporting Information) display the solar cell parameters of the $Cs_2AgBi_2I_9$ devices fabricated using the two conjugated polymers, PCPDTBT and PPDT2FBT (also see Figure S15 and Table S5, Supporting Information for the average parameter values). While both conjugated conducting polymers improved the J_{SC} values of the devices compared to Spiro-OMeTAD with J_{SC} sequence the order being PPDT2FBT > PCPDTBT > Spiro-OMeTAD, only PPDT2FBT resulted in an improvement in V_{OC} (average V_{OC} of 0.763 ± 0.025 V) compared to Spiro-OMeTAD (average V_{OC} of 0.698 ± 0.013 V). Consequently, the devices with PPDT2FBT as the HTL showed significantly better performance, with an average PCE of 2.62% ± 0.30%, compared to 1.19% ± 0.16% for Spiro-OMeTAD and 1.39% ± 0.14% for PCPDTBT HTL cells. This significantly improved performance can be attributed to the most effective energy level alignment between the valence band of $Cs_2AgBi_2I_9$ and the HOMO of the PPDT2FBT HTLs (Figure S16, Supporting Information). Notably, a maximum V_{OC} of above 0.8 V was achieved for the PPDT2FBT-containing device (Figure S15b, Supporting Information), marking one of the highest values among the best-performing bismuth halide PIMs such as Ag-Bi-I.[14,57] By contrast, HTL engineering did not result in a substantial enhancement in the performance of the CBI devices, with the PCE of the best-performing device remaining below 0.5%. Figure 4b and Figure S17 (Supporting Information) show a comparison of the PCE and other device parameter distributions between CBI and $Cs_2AgBi_2I_9$ solar cells, with the average values provided in **Table 3**.

The *J–V* curves of the champion $Cs_2AgBi_2I_9$ and CBI devices are illustrated in Figure 4c. The best-performing $Cs_2AgBi_2I_9$ device achieved a PCE of 2.92%, J_{SC} of 5.97 mA cm^{-2}, V_{OC} of 0.729 V, and FF of 67.2% (See Table S5, Supporting Information). Both the devices exhibited *J–V* hysteresis between the two scans (Figure 4c), which may be attributed to interfacial defects and ion migration.[58] Therefore, we conducted a short maximum power point tracking for obtaining the stabilized PCE of the device. The stabilized power output (SPO) measurement demonstrated a PCE of 2.87% (inset of Figure 4c), closely matching that of the value of 2.92% obtained from the *J–V* scan. The SPO trends for 30 independent devices, with corresponding PCE values ranging from 2.4% to 2.8% (Figure S18, Supporting Information), confirm the reproducibility and reliability of the device performance. The external quantum efficiency (EQE) of the champion device is 43% EQE near the absorption edge and 55%–60% at 350–400 nm (Figure S19, Supporting Information). The J_{SC} value integrated from the EQE ($J_{SC}^{\ EQE}$ = 6.30 mA cm^{-2}, see Figure S19, Supporting Information) falls within a 5% discrepancy range when compared to the value obtained from the *J–V* curves ($J_{SC}^{\ J\text{-}V}$ = 5.97 mA cm^{-2}).

We performed transient photovoltage (TPV) and electrochemical impedance spectroscopy (EIS) measurements on CBI and $Cs_2AgBi_2I_9$ devices to gain deeper insights into charge transport, recombination kinetics, and ion migration in these devices. Our TPV data and fitting outcomes (see Figure 4d; Figures S20, S21, and Table S6, Supporting Information) suggest that $Cs_2AgBi_2I_9$ devices have a lower Shockley-Read-Hall (SRH) recombination rate[59] compared to CBI. On the other hand, our EIS data analysis (refer to Figure 4e; Figure S22 and Table S7, Supporting Information) demonstrates the benefits of compositional engineering. Both interfacial and bulk recombination are suppressed due to higher recombination resistance, and slower ion migration in $Cs_2AgBi_2I_9$ devices compared to CBI devices. The detailed TPV and EIS data analysis can be found in the Note S4 (Supporting Information). Furthemore, the dominant non-radiative recombination of the charge carriers in the $Cs_2AgBi_2I_9$ devices under short-circuit and open-circuit conditions were studied by conducting light-intensity dependent (0.1–1.0 Sun) *J–V* measurements (see Note S5, Supporting Information for details and Figure S23 and Table S8, Supporting Information). Notably, the PCE increased from 2.81% to 3.41% as light intensity decreased from 1Sun to 0.1Sun (Figure 4f), mainly due to an increase in the FF from 67.2% to 72.77%, which resulted from decreased bimolecular recombination.[60] Additionally, the EQE spectrum of $Cs_2AgBi_2I_9$ aligns well with the indoor WLED emission spectrum

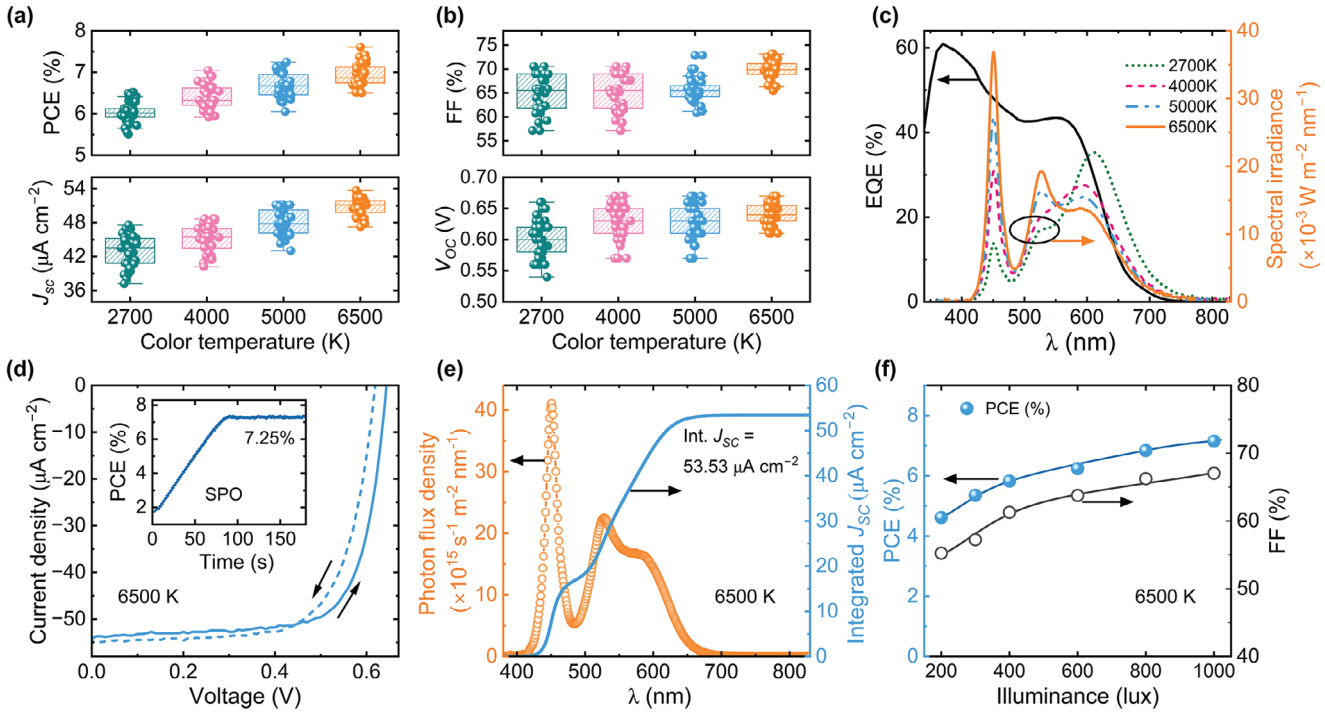

Figure 5. IPV performance of $Cs_2AgBi_2I_9$ under different WLED color temperatures and illuminances. a,b) Statistical distributions (30 independent devices) of the photovoltaic parameters of $Cs_2AgBi_2I_9$ IPV cells under different color temperatures of WLED illumination at 1000 lux. c) EQE spectrum of the champion device (left) and spectral irradiance spectra of different color temperatures of WLED at 1000 lux (right). d) *J–V* curves (reverse and forward scans) of the champion device under 1000 lux illuminance (6500 K color temperature). The arrows indicate the direction of the *J–V* scans. The inset shows the stable power output (SPO) of 7.25% of the champion device recorded at MPP voltage of 0.6 V. e) Photon flux density spectrum of WLED (6500 K color temperature) at 1000 lux (left) and the integrated J_{SC} profile of the champion device (right). (f) PCE and FF variations of a $Cs_2AgBi_2I_9$ device with WLED (6500 K color temperature) intensity, ranging 200–1000 lux.

(refer to Figure S24, Supporting Information), minimizing non-absorption losses, unlike the solar spectrum (AM 1.5 G). These findings indicate that $Cs_2AgBi_2I_9$ PV cells are well-suited for harvesting low-intensity indoor light.

A reliable IPV device should maintain consistent performance across various indoor conditions, including different color temperatures and light intensities. To this end, we investigated the impact of hole transport layers (HTLs)—PPDT2FBT, PCPDTBT, and Spiro-OMeTAD—as well as grain size on $Cs_2AgBi_2I_9$ device performance under WLED illumination at 6500 K and 1000 lux (Figures S25–S30, Tables S9 and S10, Supporting Information). Detailed analyses of these factors are provided in Notes S6 and S7 (Supporting Information). $Cs_2AgBi_2I_9$ films annealed at 225 °C for 5 min exhibited larger grain sizes, which enhanced charge collection at the electrodes, leading to improved photocurrent generation and overall device performance (Figure S28 and Table S9, Supporting Information). The device incorporating the PPDT2FBT HTL achieved superior power conversion efficiency (7.6%) compared to devices with other HTLs, under WLED illumination at a color temperature of 6500 K and 1000 lux (Figure S30 and Table S10, Supporting Information).

We further investigated the IPV performance of $Cs_2AgBi_2I_9$ devices under different color temperatures (2700, 4000, 5000, and 6500 K) of WLED at 1000 lux illuminance (the corresponding *J-V* features (See, Figure S31, Supporting Information) and power density values are given in Experimental section). The corresponding spectral irradiance or emission spectra are shown in **Figure 5c**, with power densities provided in Table S11 (Supporting Information). The intensity ratio between the blue component (≈400–500 nm) and the broad, red component (≈500–750 nm) of the WLED emission gradually decreases as the color temperature of the WLED increases from 2700 to 6500 K. The devices performed best under 6500 K, which has the strongest blue component intensity among all the color temperatures and where the EQE of the devices is the highest (Figure 5c). The statistical distributions of the IPV device parameters (J_{SC}, V_{OC}, *FF* and *PCE*) extracted from 30 independent devices are displayed in Figure 5a,b and are summarized in Table S12 (Supporting Information). Under 1000 lux illuminance of the 6500 K WLED, an average PCE of (6.92 ± 0.26)% was achieved and the devices yielded an impressive corresponding V_{OC} value of (0.641 ± 0.017) V. This is among the highest values, ranging 0.6–0.7 V, achieved at 1000 lux among the pnictogen halide PIM-based IPVs (see Table S13, Supporting Information). The improved defect tolerance of the $Cs_2AgBi_2I_9$ absorber, attributed to large polaron formation, along with the high shunt resistance on the order of 10^6 Ω cm^{-2}, (2.95×10^6 Ω cm^2 for the champion device, and an average value of $1.62 \pm 0.35\ 10^6$ Ω cm^{-2} for more than ten devices), notably reduces voltage losses under low-light intensity conditions. The *J–V* curves of champion device under 6500K color temperature of WLED illumination at 1000 lux is shown in Figure 5d. The device achieved a PCE of 7.60%,

marking the highest indoor PCE for pnictogen halide PIMs (see Table S13, Supporting Information for the comparison) under ≈300 µW cm^{-2} irradiance (1000 lux illuminance), which is the standard irradiance value for indoor testing conditions.[19,61] Notably, there was a minor mismatch of ≤3% between $J_{SC}{}^{EQE}$ of 53.55 µA cm^{-2} (Figure 5e) and $J_{SC}{}^{J\text{-}V}$ of 54.14 µA cm^{-2} (Figure 5d), confirming the excellent reliability of our indoor *J-V* measurements. Additionally, the PCE varied between 6.42% and 7.60% under different color temperatures, ranging 2700–6500 K (Figure 5a). The corresponding *J–V* curves and stabilized PCE trend are shown in Figure S31. The performance of $Cs_2AgBi_2I_9$ based device is lower than that of existing IPV technologies (Tables S13 and S14, Supporting Information). However, these IPV technologies face significant challenges, such as toxicity (lead halide perovskites), cost issues (non-fullerene acceptors in high-performing organic photovoltaics), and non-sustainable electrolytes (dye-sensitized solar cells). The indoor performance can be improved by reducing J_{SC} and V_{OC} losses in the devices.

We studied the IPV performance of a $Cs_2AgBi_2I_9$ device (7.2% PCE under 1000 lux) under varying illuminances (6500 K color temperature), ranging from 100 to 1000 lux. The corresponding *J–V* curves and PV parameters are shown in Figures S32 and S33, and the IPV device parameters are summarized in Table S15 (Supporting Information). The PCE decreased from 7.20% to 4.61% as the illuminance was reduced from 1000 to 200 lux. Notably, the device generated a V_{OC} of 0.499 V even at a very low-light intensity of 100 lux. The log(J_{SC}) versus log(p) plots for $J_{SC} \propto p^{\alpha}$ (where p is light intensity) produced $\alpha \approx 1$ (see Figure S33a, Supporting Information). The linear dependence of the photocurrent on light intensity suggests carrier trapping (monomolecular recombination) through defect states uniformly distributed in energy, and the efficient charge extraction even at very low-light intensities.[62] On the other hand, the light intensity dependency of V_{OC} is shown in Figure S33b (Supporting Information). The slope of the semi-log plot between V_{OC} and log(p) equals $n_{ID}k_BT/q$ (where n_{ID}, k_B, T, and q represent ideality factor, Boltzmann constant, temperature, and electric charge). The estimated n_{ID} values of ≈2.6 indicate that recombination primarily occurs through trap-assisted pathways involving mid-gap defect states. The reduced number of photogenerated carriers to defects decreases as the light intensity decreases, resulting in voltage and FF losses, which contribute to the PCE loss under very low-light intensity conditions. The V_{OC} and FF losses can be mitigated by enhancing the shunt resistance (which is on the order of 10^6 Ω cm^{-2}) of the devices[63,64] by an order of magnitude or more by reducing the pinholes that act as shunt pathways and addressing non-uniformities in the light-absorbing $Cs_2AgBi_2I_9$ layer (Figures S2a and S11, Supporting Information). Although the indoor PCE of $Cs_2AgBi_2I_9$ IPVs is still relatively modest, approaching 8% at 1000 lux, the intrinsic attractive features of the absorber, such as high electron dimensionality and adequate carrier mobility, large polaron size, and low electron-phonon coupling, potentially suggest a brighter future in IPVs, pending further optimization at both film and device level. To verify this potential, we calculated the indoor spectroscopically limited maximum efficiency (i-SLME)[65] for the measured absorption coefficient of $Cs_2AgBi_2I_9$, which we have adapted to consider reference indoors light sources.

In particular, we used the spectral irradiance of WLED light source at 1000 lux intensity and different color temperatures (**Figure 6**a). The i-SLME values remained the highest for 6500 K across thicknesses up to 800 nm. Beyond this point, other color temperatures yielded marginally higher performance than 6500 K. This trend aligns with the experimental PCE versus color temperature trends observed in the devices (refer to Figure 5a). A high i-SLME of ≈41% is predicted for a 6500 K color temperature with a 400 nm thick $Cs_2AgBi_2I_9$ layer (Figure 6a; Figures S34 and S35, Supporting Information), which is approximately the thickness range of $Cs_2AgBi_2I_9$ in our champion device. However, the experimentally obtained PCE of 7.60% of the champion device is lower than the theoretically predicted value. This is primarily due to the lower J_{SC} and V_{OC} experimental values versus the SLME limits (refer to Figures 5d and 6b). This issue can be attributed to the non-optimal morphology of the $Cs_2AgBi_2I_9$ layers, as evidenced by the pinholes in the top-view SEM image in Figure S2a (Supporting Information). Notably, single crystal samples of this material achieve an impressive carrier mobility-lifetime product on the order of 10^{-3} cm^2 V,$^{-1}$[32] therefore, enhancing the microstructural properties of $Cs_2AgBi_2I_9$ can improve charge transport and increase J_{SC} values. This will allow us to use a thicker $Cs_2AgBi_2I_9$ layer (≥400 nm), maximizing indoor light absorption and boosting J_{SC} values (see Figure 6a,b). Furthermore. the Urbach energy, estimated from the sub bandgap EQE spectrum[66] of the devices, is ≈70 meV (Figure 6c). This value is higher that of the LHPs[66] and explains the high V_{OC} losses in our devices. In many existing Bi- and Sb-PIMs, losses in IPV device parameters are primarily due to strong exciton-phonon coupling and high defect densities.[14] On the contrary, our experimental and theoretical results indicate that $Cs_2AgBi_2I_9$ exhibits lower exciton-phonon coupling compared to many Bi-PIMs, and the formation of large polarons enhances its defect tolerance. The low formation energy of point defects in the perovskite lattice contributes significantly to non-radiative recombination losses in $Cs_2AgBi_2I_9$. Common defects such as V_{Ag}, Bi_{Ag}, I_{Ag}, V_I, Cs_I, i_{Ag} trap or de-trap charge carriers (Figure 6d; Figures S36 and S37, Supporting Information), leading to energy loss before reaching the electrodes and affecting carrier transport. Our SCLC measurements (see, Figure S38 and Note S8, Supporting Information) confirm a defect density of 2×10^{15} cm^{-3}, highlighting the presence of grain boundary and point defects that exacerbate voltage losses. These findings are further supported by TCSPC, pump-probe data (Figure 3), EIS analysis of devices, and light-intensity dependence of device parameters, which reveal fast carrier decay components indicative of trap-assisted recombination in $Cs_2AgBi_2I_9$ thin films. To better understand the nature of these defects, we calculated the formation energies of intrinsic defects, including vacancies, cation substitutions, antistites, and interstitials (Table S16, Supporting Information). Density functional theory (DFT) analysis of intrinsic point defects in $Cs_2AgBi_2I_9$, including four vacancies (V_{Cs}, V_{Ag}, V_{Bi}, V_I), six cation substitutions (Cs_{Ag}, Cs_{Bi}, Ag_{Cs}, Ag_{Bi}, Bi_{Ag}, Bi_{Cs}), six antisites (Cs_I, Ag_I, Bi_I, I_{Cs}, I_{Ag}, I_{Bi}), and four interstitials (i_{Cs}, i_{Ag}, I_{Bi}, i_I) (refer to Table S16, Supporting Information), reveals that most defects create shallow states near the band edges. This indicates that these defects are unlikely to act as deep recombination centers, minimizing their impact on non-radiative recombination losses and overall device performance. While Bi_{Ag} creates

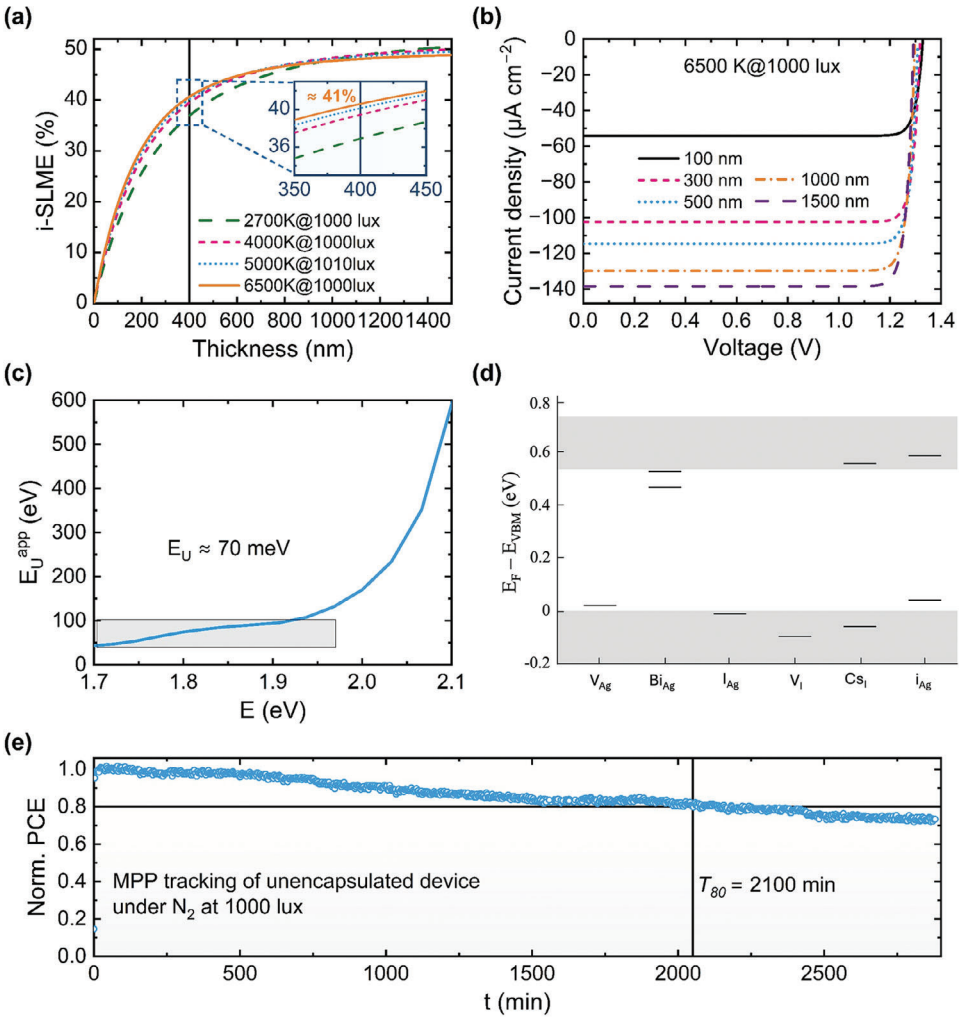

Figure 6. Theoretical efficiency limits, device performance loss analysis, and operational stability of $Cs_2AgBi_2I_9$ IPVs. a) Indoor spectroscopically limited maximum efficiency (i-SLME) of the photovoltaic efficiencies under WLED (different color temperatures) illumination of 1000 lux for $Cs_2AgBi_2I_9$ as a function of its thickness and b) the corresponding simulated *J–V* curves for different thickness values (6500 K color temperature). c) Urbach energy (E_U) estimation from the EQE spectrum using $E_U^{app} = [\frac{d}{dE} \ln(EQE)]^{-1}$.[66,67] (d) Positions of defect levels of the defected configurations of $Cs_2AgBi_2I_9$ with respect to those of VBM and CBM (shown in grey shaded areas) of the pristine system. e) Normalized PCE under indoor WLED illumination at 1000 lux in an N_2 atmosphere and at room temperature. T_{80} represents the time taken for the PCE value to reach 80% of its initial value.

states slightly below the conduction band minimum, it is unlikely to significantly contribute to non-radiative recombination. Thus, bulk defects in $Cs_2AgBi_2I_9$ are not expected to play a major role in recombination losses, with grain boundary and interface defects being the primary contributors.

Building on these insights, we propose the following strategies to minimize both J_{SC} and V_{OC} losses: 1) thin-film fabrication processes can be improved by optimizing solvents, antisolvents, precursors, and additives to enhance microstructure (increasing grain size and reduce grain boundaries), thereby suppressing bulk and interfacial recombination losses, 2) identifying ad-hoc charge transport layers to improve band alignment, reduce interfacial charge losses, and enhance charge transport,[68–71] 3) defect passivation using agents such as Lewis acids, Cl^-, or pyridine, as well as dopant modulation, can minimize defect density and reduce recombination losses, and finally, 4) advanced spectroscopic techniques, such as transient reflectance[72–74] and deep-level transient spectroscopy,[75,76] can provide a deeper understanding of defect types,[71,77] including shallow and interfacial defects, and their impact on device performance. Together, these approaches hold promise for significantly enhancing the efficiency of $Cs_2AgBi_2I_9$ IPVs under indoor conditions.

Another crucial factor for the adoption of IPVs in practical applications is the reliability of the device performance under operational conditions. Thus, we assessed the operational stability of the $Cs_2AgBi_2I_9$ IPV devices by conducting maximum power point tracking under 1000 lux illuminance in N_2 atmosphere (Figure 6e). The device maintained a stable performance with a T_{80} of over 2100 min (i.e., more than 35 h) (Figure 6e), indicating a superior performance compared to other Bi- and Sb-PIMs, which only demonstrated T_{80} values of ≈5 h or less.[78]

We attribute the enhanced stability of the $Cs_2AgBi_2I_9$ devices to two factors: the dielectric screening of photogenerated carriers by large polarons, which protects them from any deep-level defects caused by constant indoor light irradiation, and the reduced ion migration, as confirmed by our electrical characterization of the devices.

3. Conclusion

In summary, we developed polycrystalline $Cs_2AgBi_2I_9$ thin films with enhanced absorption coefficient and higher 2D dimensionality compared to well-known $Cs_3Bi_2I_9$ (CBI) perovskite-inspired material (PIM), and with a bandgap suitable for indoor light harvesting. Our theoretical calculations and spectroscopic analysis revealed large polaron formation, high mobility, and weak exciton-phonon coupling upon partial replacement of Cs with Ag at the A-site of $Cs_3Bi_2I_9$. The enhanced electron dimensionality and reduced carrier localization in $Cs_2AgBi_2I_9$, combined with HTL engineering, resulted in $Cs_2AgBi_2I_9$-based solar cells with a PCE of ≈3%. Device characterization under indoor illumination from a WLED with tunable color demonstrated a PCE of ≈7.6% (6500 K color temperature) at 1000 lux. This represents the highest value for PIM-based IPVs under ISTC irradiance (≈300 μW cm^{-2}). The corresponding power density output is 25.15 μW cm^{-2}, with a total power output of 2.5 μW. Notably, our calculations of the i-SLME limit indicate a potential efficiency of over 40% at 1000 lux for IPVs employing a $Cs_2AgBi_2I_9$ absorber. This highlights the promising future of this PIM family for indoor applications, pending further improvements in microstructure and mitigation of device losses, such as non-optimal band alignment and interfacial recombination. This work opens a new pathway for sustainable indoor light harvesting, leveraging 2D Bi-based PIMs with tunable structural and photophysical properties.

4. Experimental Section

Materials: Bismuth iodide (BiI_3, 99.99%), cesium iodide (CsI, 99.99%), hydroiodic acid (HI, 57%), chlorobenzene (CB, extra dry, 99.8%), silver iodide (AgI, 99.99%), acetonitrile (99.9%), and 4-tert-butylpyridine (4-tBP), bis(trifluoromethane)sulfonimide lithium salt (Li-TFSI, 99.95%), titanium diisopropoxide bis(acetylacetonate) 75 wt.% in 2-propanol, 2-propanol (anhydrous 99.5%), were purchased from Sigma–Aldrich. Tris[2-(1H-pyrazol-1-yl)—4-tert- butylpyridine]cobalt(III)tri[bis-(trifluoromethane) sulfonimide] (FK209 Co(III), >98%) was purchased from Dyenamo. N,N-dimethylformamide (DMF, anhydrous 99.8%), and dimethyl sulfoxide (DMSO, anhydrous 99.8%) was acquired from Alfa Aesar. 2,2′,7,7′-Tetrakis(N,N-di-p-methoxy phenylamino)—9,9 spirobifluorene (Spiro-OMeTAD) was purchased from Lumtec. Poly[(2,5-bis(2-hexyldecyloxy)phenylene)-alt-(5,6-difluoro-4,7-di(thiophen-2-yl)benzo[c] [1,2,5]thiadiazole)] (PPDT2FBT, 70–100 kg mol^{-1},) was purchased from brilliant matters. Poly[2,6-(4,4-bis-(2-ethylhexyl)-4H-cyclopenta [2,1-b;3,4-b′]dithiophene)-alt-4,7(2,1,3-benzothiadiazole)] (PCPDTBT) was purchased from 1-Material. 30NRD TiO_2 nanoparticle paste was acquired from the Greatcell Solar Materials. All the chemicals were used as received, without any further purification.

$Cs_3Bi_2I_9$ (CBI) Films and $Cs_2AgBi_2I_9$ Films: The CBI precursor solution was prepared by mixing 3 mmol of CsI and 2 mmol of BiI_3 in 1 mL of DMF:DMSO (4:1 volume ratio) solution. A 2 vol% HI solution was added to the prepared precursor solution to completely dissolve the initial precursors and to compensate for iodine evaporation during the annealing process. The precursor solution was then kept on a hot plate under magnetic stirring conditions (600 rpm) at room temperature overnight (≈12 h) inside a glove box. Next, 60 μL of the prepared CBI solution were spin-coated at 4000 rpm for 20 s on glass and mp-TiO_2 coated substrates to form a film. During the spin-coating, 150 μL of chlorobenzene antisolvent were dripped onto the rotating substrate after 6 s to form a uniform and pinhole-free perovskite film by increasing the nucleus density during film formation. Finally, the spin-coated CBI films were annealed at 130, 175, and 225 °C for 5 min on a hot plate inside a glove box to form a crystalline phase. Similarly, the $Cs_2AgBi_2I_9$ precursor solution was prepared by mixing 2 mmol of CsI, 1 mmol of AgI, and 2 mmol of BiI_3 in 1 ml of DMF:DMSO (4:1 volume ratio) solution. The same synthesis protocol used for CBI films was repeated for $Cs_2AgBi_2I_9$ film preparation. The prepared CBI and $Cs_2AgBi_2I_9$ films were adopted for to structural, morphological, chemical compositional, optical, photophysical, and photovoltaic characterizations.

Solar Cell Fabrication: The solar cells were fabricated onto pre-patterned fluorine-doped tin oxide (FTO) coated substrates (TEC15, 2.2 mm thick, from OPV Tech). The patterned substrates were cleaned by brushing with 2% Mucasol solution and water. Subsequently, the substrates were cleaned by a 15-min sonication in ultra-pure water, acetone, and 2-propanol, and dried with an N_2 flow. After that, the cleaned FTO substrates were subjected to a 15-min UV ozone treatment to remove residues of organic byproducts on their surface. A compact titanium dioxide (compact TiO_2) layer was deposited onto the cleaned and UV zone-treated FTO substrates by spray pyrolysis. The compact layer precursor solution was made by adding 1.5 mL of 75 wt.% titanium diisopropoxide bis(acetylacetonate) to 6.5 ml of 2-propanol. The precursor solution was sprayed at 450 °C onto UV ozone treated patterned FTO substrates with ten short cycles with 20 s between them. After the final cycle, the substrates were annealed for 45 min at the same temperature. The mesoporous TiO_2 (mp-TiO_2) layer was deposited by spin-coating (4000 rpm for 30 s) a 30NRD TiO_2 nanoparticle paste/ethanol solution (0.3 g/1 mL). The mp-TiO_2-coated substrates were calcinated in an oven at 450 °C for 30 min in the air and then immediately transferred into an N_2-filled glove box when their temperature was slightly above 150 °C. The CBI and $Cs_2AgBi_2I_9$ absorber thin films were deposited on top of the mp-TiO_2 substrates via spin-coating inside the N_2 glove box. 60 μL of the CBI and $Cs_2AgBi_2I_9$ precursor solution were pipetted onto the mp-TiO_2 coated substrate and then spin-coated at 4000 rpm for 20 s. During the spin-coating, 150 μL of antisolvent chlorobenzene were dripped onto the rotating substrate after 6 s. The spin-coated CBI and $Cs_2AgBi_2I_9$ films were annealed at 225 °C for 5 min on a hotplate inside the glove box. After that, solutions of 10 mg PCPDTBT and PPDT2FBT in 1 ml of 1,2-dichlorobenzene and of doped Spiro-OMeTAD in 28 mM were used as the hole transport layers (HTLs). 80 μL of doped Spiro-OMeTAD solution were spin-coated dynamically (1800 rpm for 30 s) onto the CBI and $Cs_2AgBi_2I_9$ films inside the N_2 glove box. Similarly, 60 μL of PPDT2FBT and PCPDTBT solution were spin-coated dynamically (2000 rpm for 30 s) onto the CBI and $Cs_2AgBi_2I_9$ films inside the N_2 glove box and annealed at 80 °C for 10 min. Finally, the solar cell was completed by thermally evaporating a 100 nm thick gold contact under a ≈10^{-6} mbar vacuum. Each substrate comprises eight independent solar cells (pixels) with an active area of 10 mm^2 defined by shadow mask.

XRD and Raman: High-resolution XRD patterns of the $Cs_2AgBi_2I_9$ thin films on glass substrates was performed with a Rigaku Ultima diffractometer operating at 40 kV and 40 mA, using Cu Kα radiation. The resulting patterns were analyzed with FullProf Suite software. Raman spectra were obtained using a Horiba LabRAM HR instrument with a 785 nm laser for excitation.

SEM: The top-view SEM images and cross-sectional of the $Cs_2AgBi_2I_9$ were recorded using a field emission scanning electron microscope Carl Zeiss Ultra 55 (operation was at 10 kV). EDS spectroscopy (Oxford Instruments X-MaxN 80 EDS) combined with (Zeiss UltraPlus FE-SEM) was employed to determine the elemental composition of the films.

Ultraviolet Photoelectron Spectroscopy (UPS): Ultraviolet photoelectron spectroscopy (UPS) was conducted using a PHI 5000 Versa Probe III

with a photon energy of 21.2 eV. Temperature-dependent time-correlated single-photon counting (TCSPC) measurements were performed with a Horiba Scientific Deltaflex Modular Fluorescence Lifetime System, excited with a 450 nm laser source.

UV–Vis, PL and TCSPC: UV–vis absorption spectra were collected using an Agilent Cary 5000 UV–vis–NIR spectrometer. Photoluminescence (PL) measurements at room and low temperatures were carried out using a Raman Triple Spectrometer (Jobin-Yvon T64000) with a 532 nm Nd green laser as the excitation source. Temperature-dependent TCSPC measurements were performed with a Horiba Scientific Deltaflex Modular Fluorescence Lifetime System, excited with a 450 nm laser source.

Ultrafast Transient Absorption Measurements: Ultrafast transient absorption measurements of the $Cs_2AgBi_2I_9$ thin films were conducted at room temperature using a setup with a Ti regenerative amplifier that generates 800 nm pulses with a width of 120 fs. The fundamental beam was split to generate both pump and probe beams; one portion of the beam was directed through a BBO crystal to create the pump beam at 400 nm with an average energy of ≈5 µJ. The other portion of the beam was delayed using a computer-controlled motion controller before passing through a rotating CaF_2 plate to generate a white light continuum (450–750 nm) with a pulse width of less than 120 fs, which served as the probe beam. The computerized software synchronized with detection electronics measured the change in absorbance using the equation $\Delta A = A_e - A_g$, where, $A_e = -[log(\frac{I_P^*}{I_R^*})]$ and $A_g = -[log(\frac{I_P}{I_R})]$. The probe and reference beam intensities were denoted as I_P and I_R, respectively. Here, * represents the excited state after the pump beam.

J-V Measurements: The *J-V* characteristics of the solar cells were recorded by illuminating the devices with a Sinus-70 LED-powered solar simulator from Wavelabs, set to 1-Sun (100 mW cm^{-2}) with a Newport KG5 filtered reference cell (91150-KG5 Reference Cell and Meter). The measurements were performed with a Keithley 2450 source-monitor unit using a 4-wire setup in ambient conditions. The indoor *J-V* characteristics were carried out under the illumination from a Philips HUE WLED bulb with tunable color-temperatures, including 2700, 4000, 5000, and 6500 K. The light intensity (or illuminance) of different color temperatures of the WLED bulb was adjusted/controlled by Philips Hue Essential App in the range from 100 lux to 1000 lux. The spectral irradiance and power densities of the WLED bulb with different color temperatures was determined with the help of a BTS256-WF spectral light meter (Gigahertz-Optik). The measured power densities of the illuminance of 1000 lux of different color temperatures were 322, 306, 316 and 331 µW/cm^2/nm for 2700, 4000, 5000 and 6500 K, respectively. The measured power densities of other illuminances (1000 lux to 100 lux) of 6500 K color temperature are given in Tables S17 (Supporting Information). The list of abbreviation in the revised manuscript is listed in the Table 18 (Supporting Information).

Transient Photovoltage Measurements (TPV) and Electrochemical Impedance Spectroscopy Measurements: To assess the recombination time constant of the devices, it conducted transient photovoltage measurements (TPV) using a homemade setup with a white light source having intensity of 1 Sun. The TPV spectra were fitted by a mono-exponential decay function. The electrochemical impedance spectroscopy (EIS) measurements were carried out with an Ivuum Electrochemical Workstation at 0.4 V applied bias in the dark. In EIS, an AC amplitude of 20 mV was applied, and the frequency range was varied from 0.5 MHz to 5 Hz to measure the impedance of the solar cells. The EIS data has been fitted with Zview software.

Computational Details: It conducted a comprehensive investigation into the electronic and optical properties of CBI and $Cs_2AgBi_2I_9$ using a combination of Density Functional Theory (DFT)[79,80] and Many-Body Perturbation Theory (MBPT).[81,82] Ground-state DFT calculations were performed with the QUANTUM ESPRESSO suite,[83] employing the generalized gradient approximation (GGA) as implemented in the PBE exchange-correlation (ε_{xc}) functional.[84] It utilized a plane-wave kinetic energy cutoff of 60 Ry and scalar-relativistic norm-conserving Troullier-Martins pseudopotentials.[85] The experimental geometries were optimized using the PBEsol functional,[86] which was tailored for the accurate prediction of lattice constants in systems with van der Waals interactions. The Brillouin zone was sampled using a 5 × 5 × 2 Monkhorst-Pack grid. Effective mass calculations were carried out with SUMO[87] using a parabolic fitting of the band edges. The static ionic dielectric constant was calculated using the density functional perturbation theory (DFPT).[88] Quasiparticle GW calculations and optical spectra computations were performed using the YAMBO code,[89] with quasiparticle energies computed via the single-shot GW (G_oW_o) approximation[90] and the energy dependence of the GW self-energy described using the Godby-Needs plasmon-pole model.[91] A plane-wave kinetic energy cutoff of 40 Ry (4 Ry) was used for the exchange (correlation) part of the GW self-energy. The optical absorption spectra were obtained by solving the Bethe-Salpeter equation[92,93] with scissor correction obtained using our calculated GW and DFT bandgaps. Furthermore, to investigate the interaction of the charge-carriers with the longitudinal optical phonon modes, the Fröhlich's mesoscopic model was employed.[94]

The defect calculations were performed using a 2 × 2 × 1 supercell, with energies computed using the screened hybrid exchange correlation functional proposed by Heyd, Scuseria, and Ernzerhof (HSE06).[95] 25% of Hartree -Fock and 75% of GGA-PBE contributions were used to compute the exchange part in HSE06. The defect formation energy was calculated using the following expression:

$$E_f = E_{tot}\ [X^q] - E_{tot}\ [bulk] + \sum_i n_i \mu_i + q\left(\varepsilon_{VBM} + E_f\right) \quad (3)$$

where, $E_{tot}[X^q]$ is the total energy of the defect supercell with charge q, E_{tot}[bulk] is the total energy of the perfect supercell, n_i is the number of species i added or removed from the supercell to create the defect, and μ_i is the corresponding chemical potential of species i. n_i is negative if a species was added to the system and positive if a species was removed. ε_{VBM} is the valence band maximum of the perfect supercell, and E_F is the Fermi energy of the defect supercell relative to ε_{VBM}. In this work, the electrostatic energy correction was less than 0.1.

It considered all possible point defects in $Cs_2AgBi_2I_9$, keeping the chemical potential within the stability region of the compound. The formation energies of various point defects were computed using the hybrid HSE06 ε_{xc} for four vacancies (V_{Cs}, V_{Ag}, V_{Bi}, V_I), six cation substitutions (Cs_{Ag}, Cs_{Bi}, Ag_{Cs}, Ag_{Bi}, Bi_{Ag}, Bi_{Cs}), six antisites (Cs_I, Ag_I, Bi_I, I_{Cs}, I_{Ag}, I_{Bi}), and four interstitials (i_{Cs}, i_{Ag}, I_{Bi}, i_I), as given in Table S16 (Supporting Information). Formation energies of neutral defects were obtained using the HSE06 functional.

i-SLME Limits Calculations: It calculates the SLME performance of the $Cs_2AgBi_2I_9$ material under different values of thickness, using the following key parameters. The WLED irradiance spectrum at various color temperatures (2700, 4000, 5000, and 6500 K) as demonstrated in Figure 5c for a luminescence of 1000 lux. The fundamental band gap of $Cs_2AgBi_2I_9$ was set to the single crystal value of 1.72 eV, with the first allowed dipole transition set at 1.73 eV.[32] The SLME was calculated at 300 K.

Supporting Information

Supporting Information is available from the Wiley Online Library or from the author.

Acknowledgements

M.K. and K.S. contributed equally to this work. P.V. and G.K.G. acknowledge the financial support of Jane and Aatos Erkko foundation within the SOL-TECH project. P.V. thanks Research Council of Finland, Decision No. 347772. M.K. and P.V. acknowledge the support of the SPOT-IT project founded by the CETPartnership, the Clean and Energy Transition Partnership under the 2022 CET Partnership joint call for research proposal, co-founded by the European Commission (GA 101069750) and

with the founding of the organizations detailed on https://cetpartnership.eu/funding-agencies-and-call-modules. M.K. and P.V. thank the SPINIP-HORIZON-MSCA-2023-PF-1 (Project Grant No: 101150357) for funding. C.T. and G.V. acknowledge financial support by the Agence Nationale pour la Recherche through the CPJ program and the SURFIN project (Grant No. ANR-23-CE09-0001). P.M. thanks the financial support of the Finnish Cultural Foundation (grant 00240880, Kalle & Dagmar Välimaa fund). K. D. M. R. acknowledges the Science and Engineering Research Board (SERB, CRG/2022/0048730) and UGC-DAE CRS/2022-23/01/676 projects for financial support and IACS for research facilities. K.S. acknowledges CSIR for fellowship. S.K. acknowledges UGC for fellowship. K.V.A. and A.T. gratefully acknowledge the support from the Department of Science and Technology (DST), India, through the project DST/NM/TUE/QM-8/2019(G)/1. The work is part of the Research Council of Finland Flagship Programme, Photonics Research and Innovation (PREIN), decision number 346511. This work made use of Tampere Microscopy Center facilities at Tampere University.S.M. acknowledges IIT Delhi for the senior research fellowship. S.B. acknowledges financial support from SERB under a core research grant [Grant No. CRG/2019/000647] to set up the High-Performance Computing facility "Veena" at IIT Delhi for computational resources.

Conflict of Interest

The authors declare no conflict of interest.

Author Contributions

M.K. and K.S. conducted experiments on film processing of bismuth perovskite-inspired material. K.S. performed structural analyses (XRD and Raman spectroscopy) and trap density calculations and collaborated with S.K. on low-temperature PL measurements and analyses. M.K. carried out device fabrication and characterisation under various light conditions. Additionally, M.K. conducted the FE-SEM and EDS analyses of thin films and wrote the first draft of the manuscript together with GK.G. and K.S. S.M. and S.B. conducted and analysed DFT calculations and defect analysis. K.V.A. and A.T. performed and analysed transient absorption measurements. D.M. and P.M. assisted with photovoltaic measurements. K.D.M.R. initiated the project in discussion with G. K. G. and P. V. and supervised the thin-film processing and the structural and photophysical investigations and analyses. G.K.G. and P.V. conceptualised the indoor photovoltaics study and developed the indoor characterisation methodology. P.V. managed and supervised the overall work. All authors contributed to drafting and finalising the manuscript.

Data Availability Statement

The data that support the findings of this study are available in the supplementary material of this article.

Keywords

bismuth, exciton-phonon coupling, indoor photovoltaics, perovskite-inspired material, polaron

Received: October 2, 2024
Revised: December 3, 2024
Published online: December 26, 2024

[1] M. Ataei, M. Adelifard, S. S. Hosseini, *J. Electron. Mater.* **2021**, *50*, 571.
[2] M. Hayes, G. Fagas, J. Donnelly, R. Salot, G. Savelli, P. Spies, G. vom Boegel, M. Konijnenburg, D. Stenzel, A. Romani, C. Gerbaldi, F. Cottone, A. Weddell, "EnABLES Position Paper coordinated by Tyndall recommends key actions to power IoT in a reliable and sustainable way-Research Infrastructure to Power the Internet of Things".
[3] B. Zhang, J. C. Bonner, L. N. S. Murthy, T. A. Nguyen, F.-Y. Cao, Y.-J. Cheng, B. H. Hamadani, J. W. P. Hsu, *Org. Electron.* **2022**, *104*, 106477.
[4] N. Talbanova, T. Komaricheva, L. O. Luchnikov, G. Ermolaev, V. Kurichenko, D. S. Muratov, A. Arsenin, I. S. Didenko, V. Volkov, I. V. Badurin, M. V. Ryabtseva, N. T. Vagapova, D. Saranin, A. Di Carlo, *Sol. Energy Mater. Sol. Cells* **2023**, *254*, 112284.
[5] B. H. Hamadani, M. B. Campanelli, *IEEE J. Photovolt.* **2020**, *10*, 1119.
[6] H. Yin, J. K. W. Ho, S. H. Cheung, R. J. Yan, K. L. Chiu, X. Hao, S. K. So, *J. Mater. Chem. A* **2018**, *6*, 8579.
[7] A. Chakraborty, G. Lucarelli, J. Xu, Z. Skafi, S. Castro-Hermosa, A. B. Kaveramma, R. G. Balakrishna, T. M. Brown, *Nano Energy* **2024**, *128*, 109932.
[8] J. Park, J. Kim, H.-S. Yun, M. J. Paik, E. Noh, H. J. Mun, M. G. Kim, T. J. Shin, S. I. Seok, *Nature* **2023**, *616*, 724.
[9] Q. Ma, Y. Wang, L. Liu, P. Yang, W. He, X. Zhang, J. Zheng, M. Ma, M. Wan, Y. Yang, C. Zhang, T. Mahmoudi, S. Wu, C. Liu, Y.-B. Hahn, Y. Mai, *Energy Environ. Sci.* **2024**, *17*, 1637.
[10] Z. Guo, A. K. Jena, T. Miyasaka, *ACS Energy Lett.* **2023**, *8*, 90.
[11] https://sauletech.com/rohs-compliance-tests-at-our-company.
[12] N. Moody, S. Sesena, D. W. deQuilettes, B. D. Dou, R. Swartwout, J. T. Buchman, A. Johnson, U. Eze, R. Brenes, M. Johnston, C. L. Haynes, V. Bulović, M. G. Bawendi, *Joule* **2020**, *4*, 970.
[13] Y. Peng, T. N. Huq, J. Mei, L. Portilla, R. A. Jagt, L. G. Occhipinti, J. L. MacManus-Driscoll, R. L. Z. Hoye, V. Pecunia, *Adv. Energy Mater.* **2021**, *11*, 2002761.
[14] G. K. Grandhi, D. Hardy, M. Krishnaiah, B. Vargas, B. Al-Anesi, M. P. Suryawanshi, D. Solis-Ibarra, F. Gao, R. L. Z. Hoye, P. Vivo, *Adv. Funct. Mater.* **2024**, *34*, 2307441.
[15] K. Ruhle, M. Kasemann, in *2013 IEEE 39th Photovoltaic Specialists Conf. (PVSC)*, IEEE, Tampa, FL, USA **2013**, pp. 2651–2654.
[16] R. Mohan, *Nat. Chem.* **2010**, *2*, 336.
[17] Y. Cui, L. Hong, T. Zhang, H. Meng, H. Yan, F. Gao, J. Hou, *Joule* **2021**, *5*, 1016.
[18] D. Lübke, P. Hartnagel, J. Angona, T. Kirchartz, *Adv. Energy Mater.* **2021**, *11*, 2101474.
[19] D. E. Parsons, G. Koutsourakis, J. C. Blakesley, *APL Energy* **2024**, *2*, 016110.
[20] I. Turkevych, S. Kazaoui, N. Shirakawa, N. Fukuda, *Jpn. J. Appl. Phys.* **2021**, *60*, SCCE06.
[21] N. Lamminen, G. K. Grandhi, F. Fasulo, A. Hiltunen, H. Pasanen, M. Liu, B. Al-Anesi, A. Efimov, H. Ali-Löytty, K. Lahtonen, P. Mäkinen, A. Matuhina, A. B. Muñoz-García, M. Pavone, P. Vivo, *Adv. Energy Mater.* **2023**, *13*, 2203175.
[22] N. B. Correa Guerrero, Z. Guo, N. Shibayama, A. K. Jena, T. Miyasaka, *ACS Appl. Energy Mater.* **2023**, *6*, 10274.
[23] G. K. Grandhi, B. Al-Anesi, H. Pasanen, H. Ali-Löytty, K. Lahtonen, S. Granroth, N. Christian, A. Matuhina, M. Liu, A. Berdin, V. Pecunia, P. Vivo, *Small* **2022**, *18*, 2203768.
[24] G. K. Grandhi, S. Toikkonen, B. Al-Anesi, V. Pecunia, P. Vivo, *Sustain. Energy Fuels* **2023**, *7*, 66.
[25] B. Al-Anesi, G. K. Grandhi, A. Pecoraro, V. Sugathan, N. S. M. Viswanath, H. Ali-Löytty, M. Liu, T.-P. Ruoko, K. Lahtonen, D. Manna, S. Toikkonen, A. B. Muñoz-García, M. Pavone, P. Vivo, *Small* **2023**, *19*, 2303575.
[26] S. R. Rondiya, R. A. Jagt, J. L. MacManus-Driscoll, A. Walsh, R. L. Z. Hoye, *Appl. Phys. Lett.* **2021**, *119*, 220501.
[27] L. R. V. Buizza, L. M. Herz, *Adv. Mater.* **2021**, *33*, 2007057.

[28] Y. Yamada, Y. Kanemitsu, *NPG Asia Mater* **2022**, *14*, 48.
[29] H. Zhang, N.-G. Park, *J. Phys. Energy* **2023**, *5*, 024002.
[30] F. Cesare, R. Michele, S. Martin, D. Ulrike, *Nat. Rev. Mater.* **2021**, *6*, 560.
[31] D. Bao, Q. Chang, B. Chen, X. Chen, H. Sun, Y. M. Lam, D. Zhao, J.-X. Zhu, E. E. M. Chia, *PRX Energy* **2023**, *2*, 013001.
[32] M. Hossain, K. Singh, A. Narwal, M. S. Sheikh, S. K. Reddy, K. Vankayala, A. Singh, S. Khan, S. Khan, P. K. Velpula, M. Chirumamilla, S. S. R. K. C. Yamijala, G. K. Grandhi, P. Vivo, K. D. M. Rao, *Chem. Mater.* **2024**, *36*, 7781.
[33] P. Acharyya, K. Pal, A. Ahad, D. Sarkar, K. S. Rana, M. Dutta, A. Soni, U. V. Waghmare, K. Biswas, *Adv. Funct. Mater.* **2023**, *33*, 2304607.
[34] F. Zheng, L. Wang, *Energy Environ. Sci.* **2019**, *12*, 1219.
[35] T. Holstein, *Ann. Phys.* **1959**, *8*, 343.
[36] S. Shcherbachenko, O. Astakhov, Z. Liu, L. Kin, C. Zahren, U. Rau, T. Kirchartz, T. Merdzhanova, *Adv. Energy Sustain. Res.* **2024**, *5*, 2400032.
[37] W. Tao, C. Zhang, Q. Zhou, Y. Zhao, H. Zhu, *Nat. Commun.* **2021**, *12*, 1400.
[38] Y. Zhang, C.-C. Zhang, C.-H. Gao, M. Li, X.-J. Ma, Z.-K. Wang, L.-S. Liao, *Sol. RRL* **2019**, *3*, 1800269.
[39] R. P. Feynman, *Phys. Rev.* **1955**, *97*, 660.
[40] M. Baranowski, A. Nowok, K. Galkowski, M. Dyksik, A. Surrente, D. Maude, M. Zacharias, G. Volonakis, S. D. Stranks, J. Even, M. Maczka, R. Nicholas, P. Plochocka, *ACS Energy Lett.* **2024**, *9*, 2696.
[41] R. W. Hellwarth, I. Biaggio, *Phys. Rev. B* **1999**, *60*, 299.
[42] T. D. Schultz, *Phys. Rev.* **1959**, *116*, 526.
[43] Y. Ōsaka, *Prog. Theor. Phys.* **1959**, *22*, 437.
[44] J.-P. Correa-Baena, L. Nienhaus, R. C. Kurchin, S. S. Shin, S. Wieghold, N. T. Putri Hartono, M. Layurova, N. D. Klein, J. R. Poindexter, A. Polizzotti, S. Sun, M. G. Bawendi, T. Buonassisi, *Chem. Mater.* **2018**, *30*, 3734.
[45] O. Stroyuk, O. Raievska, A. Osvet, J. Hauch, C. J. Brabec, *J. Mater. Chem. C* **2023**, *11*, 4328.
[46] Z. Zhao, M. Zhong, W. Zhou, Y. Peng, Y. Yin, D. Tang, B. Zou, *J. Phys. Chem. C* **2019**, *123*, 25349.
[47] M. T. Trinh, X. Wu, D. Niesner, X.-Y. Zhu, *J. Mater. Chem. A* **2015**, *3*, 9285.
[48] S. A. Bretschneider, F. Laquai, M. Bonn, *J. Phys. Chem. C* **2017**, *121*, 11201.
[49] Z. Guo, Y. Wan, M. Yang, J. Snaider, K. Zhu, L. Huang, *Science* **2017**, *356*, 59.
[50] S. A. Bretschneider, I. Ivanov, H. I. Wang, K. Miyata, X. Zhu, M. Bonn, *Adv. Mater.* **2018**, *30*, 1707312.
[51] K. Miyata, T. L. Atallah, X.-Y. Zhu, *Sci. Adv.* **2017**, *3*, 1701469.
[52] D. Niesner, H. Zhu, K. Miyata, P. P. Joshi, T. J. S. Evans, B. J. Kudisch, M. T. Trinh, M. Marks, X.-Y. Zhu, *J. Am. Chem. Soc.* **2016**, *138*, 15717.
[53] X. Chen, M. Jia, W. Xu, G. Pan, J. Zhu, Y. Tian, D. Wu, X. Li, Z. Shi, *Adv. Opt. Mater.* **2023**, *11*, 2202153.
[54] C. W. Koh, J. H. Heo, M. A. Uddin, Y.-W. Kwon, D. H. Choi, S. H. Im, H. Y. Woo, *ACS Appl. Mater. Interfaces* **2017**, *9*, 43846.
[55] H. C. Weerasinghe, N. Macadam, J.-E. Kim, L. J. Sutherland, D. Angmo, L. W. T. Ng, A. D. Scully, F. Glenn, R. Chantler, N. L. Chang, M. Dehghanimadvar, L. Shi, A. W. Y. Ho-Baillie, R. Egan, A. S. R. Chesman, M. Gao, J. J. Jasieniak, T. Hasan, D. Vak, *Nat. Commun.* **2024**, *15*, 1656.
[56] S. H. Im, C.-S. Lim, J. A. Chang, Y. H. Lee, N. Maiti, H.-J. Kim, Md. K. Nazeeruddin, M. Grätzel, S. I. Seok, *Nano Lett.* **2011**, *11*, 4789.
[57] A. Chakraborty, N. Pai, J. Zhao, B. R. Tuttle, A. N. Simonov, V. Pecunia, *Adv. Funct. Mater.* **2022**, *32*, 2203300.
[58] J. Thiesbrummel, S. Shah, E. Gutierrez-Partida, F. Zu, F. Peña-Camargo, S. Zeiske, J. Diekmann, F. Ye, K. P. Peters, K. O. Brinkmann, P. Caprioglio, A. Dasgupta, S. Seo, F. A. Adeleye, J. Warby, Q. Jeangros, F. Lang, S. Zhang, S. Albrecht, T. Riedl, A. Armin, D. Neher, N. Koch, Y. Wu, V. M. Le Corre, H. Snaith, M. Stolterfoht, *Nat. Energy* **2024**, *9*, 664.
[59] J.-P. Correa-Baena, S.-H. Turren-Cruz, W. Tress, A. Hagfeldt, C. Aranda, L. Shooshtari, J. Bisquert, A. Guerrero, *ACS Energy Lett.* **2017**, *2*, 681.
[60] X. Xu, W. Liu, X. Luo, H. Chen, Q. Wei, J. Yuan, Y. Zou, *ChemSusChem* **2021**, *14*, 3428.
[61] IEC Technical Specification 62607-7-2 "IEC TS 62607-7-2:2023-Nanomanufacturing - Key control characteristics - Part 7-2: Nano-enabled photovoltaics - Device evaluation method for indoor light".
[62] V. Pecunia, Y. Yuan, J. Zhao, K. Xia, Y. Wang, S. Duhm, L. Portilla, F. Li, *Nano-Micro Lett.* **2020**, *12*, 27.
[63] C. M. Proctor, T.-Q. Nguyen, *Appl. Phys. Lett.* **2015**, *106*, 083301.
[64] D. Glowienka, Y. Galagan, *Adv. Mater.* **2022**, *34*, 2105920.
[65] B. Cucco, L. Pedesseau, C. Katan, J. Even, M. Kepenekian, G. Volonakis, *Sol. RRL* **2022**, *6*, 2200718.
[66] S. Zeiske, O. J. Sandberg, N. Zarrabi, C. M. Wolff, M. Raoufi, F. Peña-Camargo, E. Gutierrez-Partida, P. Meredith, M. Stolterfoht, A. Armin, *J. Phys. Chem. Lett.* **2022**, *13*, 7280.
[67] C. Kaiser, O. J. Sandberg, N. Zarrabi, W. Li, P. Meredith, A. Armin, *Nat. Commun.* **2021**, *12*, 3988.
[68] P. Chen, Y. Bai, L. Wang, *Small Struct.* **2021**, *2*, 2000050.
[69] X. Zhang, W. Qiu, S. Apergi, S. Singh, P. Marchezi, W. Song, C. Sternemann, K. Elkhouly, D. Zhang, A. Aguirre, T. Merckx, A. Krishna, Y. Shi, A. Bracesco, C. Van Helvoirt, F. Bens, V. Zardetto, J. D'Haen, A. Yu, G. Brocks, T. Aernouts, E. Moons, S. Tao, Y. Zhan, Y. Kuang, J. Poortmans, *ACS Energy Lett.* **2023**, *8*, 2532.
[70] W. Zhang, X. Guo, Z. Cui, H. Yuan, Y. Li, W. Li, X. Li, J. Fang, *Adv. Mater.* **2024**, *36*, 2311025.
[71] D. Luo, R. Su, W. Zhang, Q. Gong, R. Zhu, *Nat. Rev. Mater.* **2019**, *5*, 44.
[72] Y. Yang, M. Yang, D. T. Moore, Y. Yan, E. M. Miller, K. Zhu, M. C. Beard, *Nat. Energy* **2017**, *2*, 16207.
[73] Y. Yang, Y. Yan, M. Yang, S. Choi, K. Zhu, J. M. Luther, M. C. Beard, *Nat. Commun.* **2015**, *6*, 7961.
[74] M. Feng, S. Ye, Y. Guo, T. C. Sum, *Nano Lett.* **2022**, *22*, 7195.
[75] S. Heo, G. Seo, Y. Lee, D. Lee, M. Seol, J. Lee, J.-B. Park, K. Kim, D.-J. Yun, Y. S. Kim, J. Kwang Shin, T. Kyu Ahn, M. Khaja Nazeeruddin, *Energy Environ. Sci.* **2017**, *10*, 1128.
[76] S. Reichert, J. Flemming, Q. An, Y. Vaynzof, J.-F. Pietschmann, C. Deibel, *Phys. Rev. Appl.* **2020**, *13*, 034018.
[77] J. M. Ball, A. Petrozza, *Nat. Energy* **2016**, *1*, 16149.
[78] G. K. Grandhi, L. Krishnan Jagadamma, V. Sugathan, B. Al-Anesi, D. Manna, P. Vivo, *Chem. Commun.* **2023**, *59*, 8616.
[79] W. Kohn, L. J. Sham, *Phys. Rev.* **1965**, *140*, A1133.
[80] P. Hohenberg, W. Kohn, *Phys. Rev.* **1964**, *136*, B864.
[81] P. Basera, S. Saini, S. Bhattacharya, *J. Mater. Chem. C* **2019**, *7*, 14284.
[82] H. Jiang, P. Rinke, M. Scheffler, *Phys. Rev. B* **2012**, *86*, 125115.
[83] P. Giannozzi, S. Baroni, N. Bonini, M. Calandra, R. Car, C. Cavazzoni, D. Ceresoli, G. L. Chiarotti, M. Cococcioni, I. Dabo, A. Dal Corso, S. de Gironcoli, S. Fabris, G. Fratesi, R. Gebauer, U. Gerstmann, C. Gougoussis, A. Kokalj, M. Lazzeri, L. Martin-Samos, N. Marzari, F. Mauri, R. Mazzarello, S. Paolini, A. Pasquarello, L. Paulatto, C. Sbraccia, S. Scandolo, G. Sclauzero, A. P. Seitsonen, et al., *J. Phys. Condens. Matter* **2009**, *21*, 395502.
[84] J. P. Perdew, K. Burke, M. Ernzerhof, *Phys. Rev. Lett.* **1996**, *77*, 3865.
[85] N. Troullier, J. L. Martins, *Phys. Rev. B* **1991**, *43*, 1993.
[86] J. P. Perdew, A. Ruzsinszky, G. I. Csonka, O. A. Vydrov, G. E. Scuseria, L. A. Constantin, X. Zhou, K. Burke, *Phys. Rev. Lett.* **2008**, *100*, 136406.
[87] A. M. Ganose, A. J. Jackson, D. O. Scanlon, *J. Open Source Softw.* **2018**, *3*, 717.

[88] M. Gajdoš, K. Hummer, G. Kresse, J. Furthmüller, F. Bechstedt, *Phys. Rev. B* **2006**, *73*, 045112.
[89] A. Marini, C. Hogan, M. Grüning, D. Varsano, *Comput. Phys. Commun.* **2009**, *180*, 1392.
[90] M. S. Hybertsen, S. G. Louie, *Phys. Rev. B* **1986**, *34*, 5390.
[91] R. W. Godby, R. J. Needs, *Phys. Rev. Lett.* **1989**, *62*, 1169.
[92] G. Onida, L. Reining, A. Rubio, *Rev. Mod. Phys.* **2002**, *74*, 601.
[93] F. Fuchs, C. Rödl, A. Schleife, F. Bechstedt, *Phys. Rev. B* **2008**, *78*, 085103.
[94] H. Fröhlich, *Adv. Phys.* **1954**, *3*, 325.
[95] A. V. Krukau, O. A. Vydrov, A. F. Izmaylov, G. E. Scuseria, *J. Chem. Phys.* **2006**, *125*, 224106.